Gypsum Precipitating From Volcanic Effluent as an Archive of Volcanic Activity

Vincent J. van Hinsberg[1]*, Kim Berlo[1], Daniele L. Pinti[2] and Bassam Ghaleb[2]

[1]GEOTOP Research Center, Department of Earth and Planetary Sciences, McGill University, Montreal, QC, Canada, [2]GEOTOP Research Center, Département des Sciences de la Terre et de l'atmosphère, Université de Québec à Montréal, Montreal, QC, Canada

Records of volcanic activity are a key resource in volcano monitoring and hazard mitigation. The time period for which such records are available and the level of detail vary widely among volcanic centers and there is, therefore, a need for supplementary sources of this information. Here, we use growth-zoned gypsum as a mineral archive of the activity of Kawah Ijen volcano in East-Java, Indonesia. Gypsum precipitates where water seeps from the crater lake and hydrothermal system, and it has formed a 100 m long cascading plateau. A 19 cm plateau cross-section was analysed for minor and trace elements using laser-ablation ICP-MS. Absolute ages were assigned to this transect based on ^{210}Pb dating. This ^{210}Pb age model was corrected for variations in the ^{210}Pb$_0$ resulting from fluctuations in the volcanic radon flux by using ^{84}Kr/^{36}Ar and ^{132}Xe/^{36}Ar. The age model indicates that the transect covers a period from 1919 ± 12 to 2008 ± 0.2. Gypsum-fluid partition coefficients (D) permit the gypsum compositions to be converted to the concentrations in the fluid from which each growth zone grew. The D-values also show the compatibility of the elements in the gypsum structure, and identify the LREE, Sr, Pb, Tl, Ni, Co, Cu, Zn, Cd, Sb, Th, and Mo as least susceptible to contamination from rock fragment and mineral inclusions, and therefore as most reliable elements of the gypsum record. Compositional variability in the timeseries correlates with known element behavior in the Kawah Ijen system and shows three element groups: the LREE, Sr, and Pb that represent rock-leaching; Cu, Zn, and Cd, which have previously been linked to immiscible sulfide destabilization in a deep-seated basalt; and Sb, Tl, and As which point to a contribution from the shallow system and evolved magma. Moreover, the gypsum record shows that episodes of unrest and quiescence have a distinct compositional signature in Kawah Ijen seepage fluids, and can be distinguished. Thus, we show that gypsum is a sensitive recorder of volcanic activity and can provide detailed information on the state of the magmatic-hydrothermal system in the past.

Keywords: gypsum, Kawah Ijen, crater lake, magmatic-hydrothermal system, volcano monitoring, element partitioning, historical record., trace elements

INTRODUCTION

Growth-zoned mineral precipitates are powerful archives of the conditions and compositions of their growth environment, and the changes therein over time. Stalactites and stalagmites of carbonates and sulfates provide information on past climate (e.g., Goede and Vogel 1991; Gazquez et al., 2020). Similarly, precipitates formed in volcanic settings can provide information on element fluxes and their variability, e.g., travertine as a recorder of volcanic CO_2 emissions (Capezzuoli et al., 2014), and gypsum stalactites have been shown to preserve an archive of physical disturbances in a volcanic setting, i.e., volcanic seismicity (Utami et al., 2019). The main benefit of these mineral archives is their ability to provide information on time periods well before historical records are available.

Minerals precipitating under equilibrium conditions incorporate minor and trace elements following their equilibrium mineral-fluid element partition coefficients, which in turn are controlled by the mineral crystal structure (cf. (Blundy and Wood, 2003; van Hinsberg et al., 2010a). This mineral-lattice control is diminished for disequilibrium growth, but as long as precipitation takes place under constant conditions, the element distribution between mineral and fluid can remain constant as well. A constant element distribution between mineral and fluid permits for the composition of the fluid to be recorded by the mineral in a predictable fashion. Where the process or parameter of interest has a characteristic compositional signature, the variability in this variable can be reconstructed by later interrogation of the mineral record (assuming compositional preservation of the precipitate). Moreover, multiple variables can be investigated at the same time when each has its own isotopic or elemental fingerprint.

Here, we investigate the use of growth-zoned gypsum, precipitated from fluids seeping from the Kawah Ijen volcano in Indonesia, as an archive of the volcanic activity of this system. In this approach, we build upon our earlier work for a Kawah Ijen gypsum stalactite reported in Utami et al. (2019), in which it was shown that gypsum composition is sensitive to fluctuations in its formation fluid. These compositional variations could in turn be linked to changes in the activity of the Kawah Ijen system, in particular an input of rock-derived elements linked to increased rockfalls and landslides as a result of physical disturbances in the system (e.g., seismicity). Utami et al. (2019) also showed that gypsum linked to the 1817 phreatomagmatic eruption of Kawah Ijen has a markedly different composition, with a strong magmatic signature. In this contribution, we aim to extend the timeseries further back in time and bridge the gap between the stalactite record (1970–2009) and the 1817 gypsum, and to improve our understanding of element partitioning between gypsum and fluid to ground-truth its use as a compositional monitor of volcanic activity.

This approach is particularly pertinent for Kawah Ijen because the historical record of its activity is incomplete and consists of only punctuated reports with variable levels of detail. Mineral archives can provide the ability to verify the available historical record, permit comparing the reports of unrest to establish a consistent and leveled record of activity, and extend the record to beyond the time period for which historical accounts are available.

GEOLOGICAL SETTING

Kawah Ijen Volcano

Kawah Ijen volcano is a passively degassing stratovolcano located within the Ijen caldera complex of East Java (**Figure 1**). It is positioned on the inner flank of the Merapi caldera rim volcano and it is the only currently active center in the caldera complex (Kemmerling, 1921; Caudron et al., 2015b). Kawah Ijen has erupted magmatic products of basaltic to dacitic bulk compositions (Handley et al., 2007; Kemmerling, 1921; Lowenstern et al., 2018; Sitorus, 1990; van Hinsberg et al., 2010b; 2017), including lavaflows, scoria and ash fall deposits, and pyroclastic flow deposits that extend in age to >21 kyr BP (Sitorus, 1990). The most recent magmatic eruption of Kawah Ijen volcano took place in 1817 (Oudgast, 1820; Bosch, 1858), but phreatic eruptions and steam explosions are common (Caudron et al., 2015a; 2015b), and fumaroles on the western lake shore emit ~200 ton/day of SO_2 in passive degassing (Vigouroux, 2011; Gunawan et al., 2016; van Hinsberg et al., 2017).
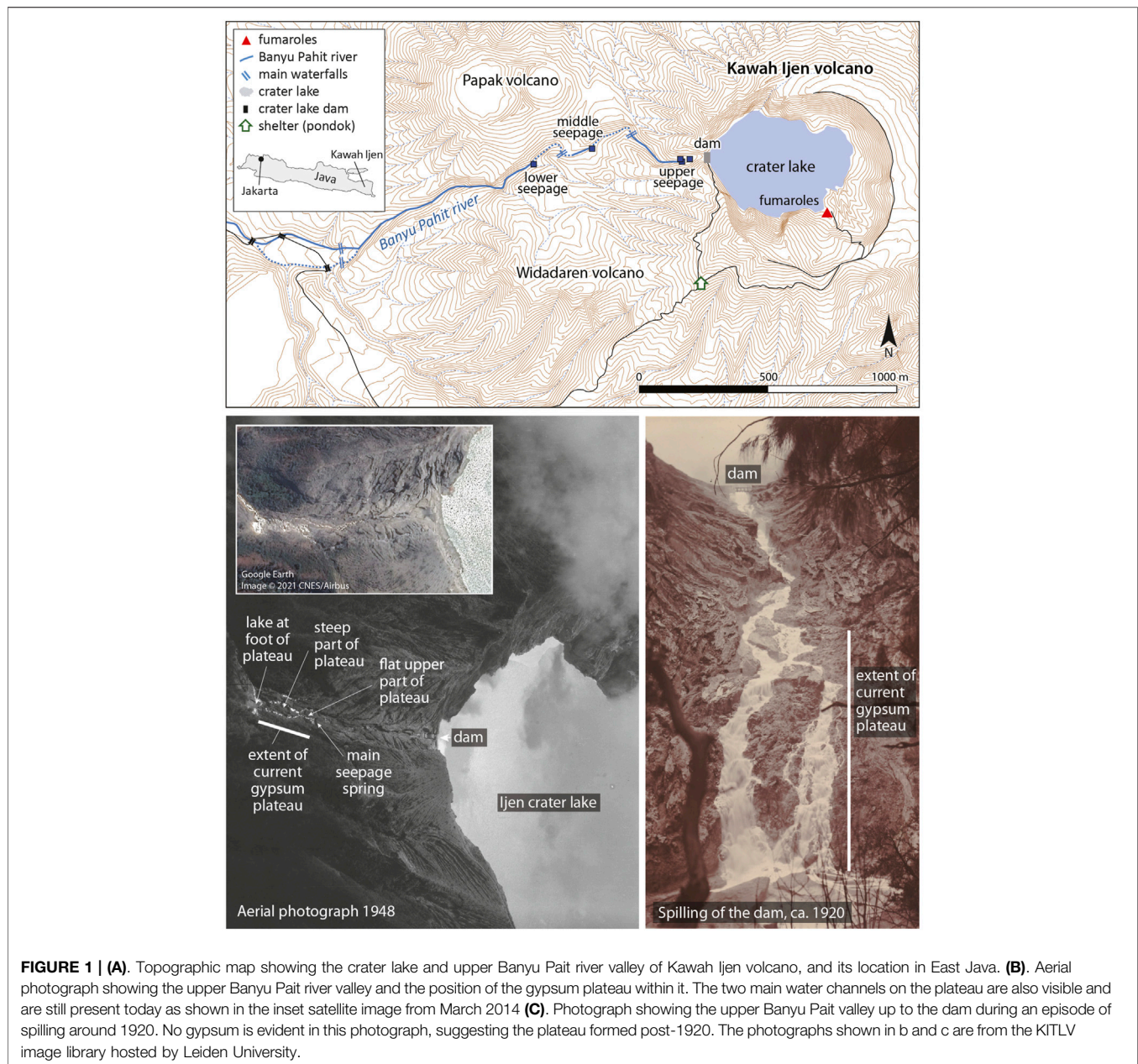
The summit crater of the volcano is occupied by a large lake (27 million m^3—Caudron et al., 2015b). The lake waters are warm hyperacidic SO_4-Cl brines with a pH ~ 0, T = 40 ± 10°C and TDS = 100 g/kg (Delmelle and Bernard, 1994; Takano et al., 2000; Caudron et al., 2015b; van Hinsberg et al., 2017). A lake has occupied the crater since at least 1796 (de la Tour, 1805; Oudgast, 1820), although it was expelled in the 1817 eruption (Bosch, 1858). The lake water composition reflects inputs from the magmatic-hydrothermal system, rainwater, and rock alteration, with mineral precipitation, evaporation and seepage as the main output fluxes (van Hinsberg et al., 2017).

In the late 19th century, a dam was built to control lake outflow (Hengeveld, 1920), with the most recent iteration of this dam still in place today. Up to the 1980s, water was periodically released from the lake to lower its level and avoid detrimental effects where the lake effluent reached irrigation systems in the Asambagus plain (see Hengeveld, 1920; van Rotterdam-Los et al., 2008; Yudiantoro et al., 2020). Since then, the level of the lake has dropped significantly, and now stands well below the level of the dam (Caudron et al., 2015b).

The compositions of melt inclusions and gas and fluid emissions from Kawah Ijen indicates the presence of two magma bodies: A deep-seated mafic magma that contributes CO_2 and a metal signature related to sulfide-liquid breakdown, and; A shallow, evolved magma characterized by elevated concentrations of semi-metals (Berlo et al., 2014). These magmatic sources are modified by interaction with the hydrothermal system and resultant element scrubbing (cf. Symonds et al., 2001), and transient mineral precipitation (van Hinsberg et al., 2017; Berlo et al., 2020).

Gypsum Deposits at Kawah Ijen

Acidic waters emerge on the western flanks of the volcano in a series of springs along the Banyu Pait river valley (**Figure 1**). The

FIGURE 1 | (A). Topographic map showing the crater lake and upper Banyu Pait river valley of Kawah Ijen volcano, and its location in East Java. **(B)**. Aerial photograph showing the upper Banyu Pait river valley and the position of the gypsum plateau within it. The two main water channels on the plateau are also visible and are still present today as shown in the inset satellite image from March 2014 **(C)**. Photograph showing the upper Banyu Pait valley up to the dam during an episode of spilling around 1920. No gypsum is evident in this photograph, suggesting the plateau formed post-1920. The photographs shown in b and c are from the KITLV image library hosted by Leiden University.

uppermost springs are dominantly lake seepage, with an increasing contribution of effluent from the hydrothermal system in springs further downstream (Palmer, 2009). The lower seepage springs are the main source of the Banyu Pait River, and river flow is continuous from this seepage area. Gypsum precipitates are found at all springs, and along the riverbed of the Banyu Pait River up to the 3rd set of springs. Gypsum precipitation is most extensive at the uppermost springs with a 100 m long cascading plateau ending in a gypsum-covered lake (**Figure 2**).

The gypsum plateau consists of a more or less flat area at the top with water flowing onto this from several small springs at the upper plateau edge (**Figures 2C,F, 3A**), and a spring with larger discharge that emerges upstream of the plateau (**Figures 2C,D**).

Gypsum covered steps descend from this flat area with a thin film of water flowing over these. The main flow shifts from the center of the plateau to the left (north) on this steep section, with most of the discharged water descending a lavaflow at the edge of the plateau in a series of small ponds rimmed by gypsum (**Figure 2B**). This lavaflow appears to continue underneath the gypsum adjacent, and may be the cause for the steep valley topography. An additional seepage spring is present on the southern edge (**Figure 2B**) with water flow initially in a channel on scoria before creating the southern gypsum plateau extension and discharging onto the gypsum-covered lake at the foot of the plateau. This lake cover is a thick crust of gypsum, although the extent of this cover downstream varied between 2007 and 2015. Two small seepage springs are present upstream
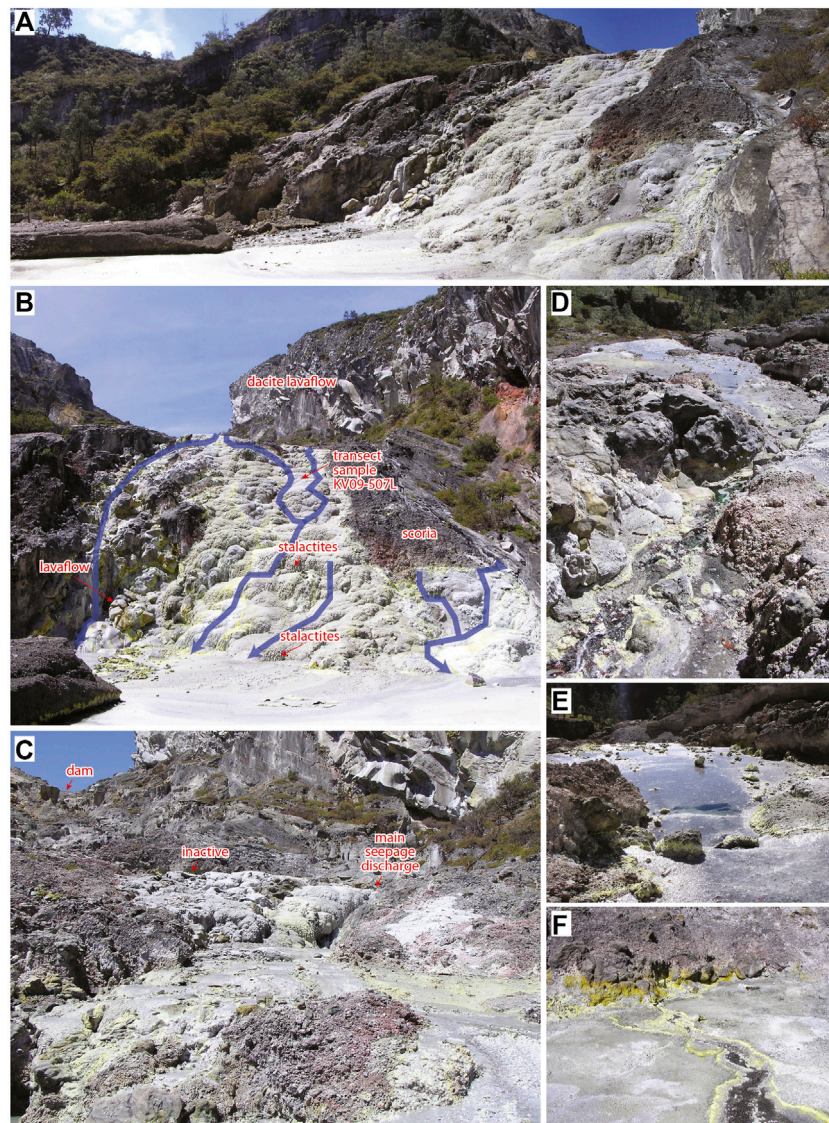
FIGURE 2 | Overview photographs of the gypsum plateau. **(A,B)**. View of the plateau looking approximately north-east and east, respectively, showing its stepped cascade shape. Gypsum stalactites grow from the overhangs of the steps. The main flow over the plateau is on the left, along the exposed lavaflow, the right center, over the sample site, and from a spring on the right that has produced the gypsum starting about two-thirds down the face on the right. **(C)**. View of the uppermost section of the plateau (not visible in a,b). The main seepage spring is on the right in this image and forms a channel with subsequent spreading out of water over the flat section of gypsum in the foreground. The white, fractured crusts of gypsum on the left represent an inactive section of the plateau. **(D)**. View towards the west from the main seepage spring above the plateau. Only small amounts of gypsum precipitate at the seepage outlets and the water flows on sediment instead. **(E)**. View of the top, flat part of the gypsum plateau looking west showing the thin film of water that covers the gypsum. **(F)**. Channel of seepage water with yellow (Na,K)-alum precipitates on either side, resulting from evaporation of spray.

of the plateau, and have gypsum and (Na,K)-alum precipitates, but water flow does not continue to the main plateau. Water outflow from the various plateau seepage springs has a temperature of 30–37°C (measured August 5th, 2009 with an ambient air temperature of 17°C).

The seepage fluids are not saturated in gypsum where they emerge, but reach saturation by cooling and evaporative concentration (Delmelle and Bernard, 2000; Utami et al., 2019). This is evidenced in the field by gypsum-free channels at the seepage outlets and initial flow on a streambed of (altered)

volcaniclastic material (**Figure 2D**). Flow is, moreover, channelized on the uppermost part of the plateau, with gypsum growing as "cauliflower" domes above the fluid level from spray (**Figures 2F**, **3A**). Where gypsum saturation is reached, the fluid spreads out into a thin sheet that covers a flat, but rough surface of gypsum laths, both on the horizontal parts of the plateau and on the steps (**Figures 2E,F**, **3A,C,D**). The laths mostly grow vertically and are dominantly 1 to 2 mm in diameter. Larger gypsum laths are found on the sides of channels and ponds growing inward (**Figure 3B**). Radial growth of gypsum
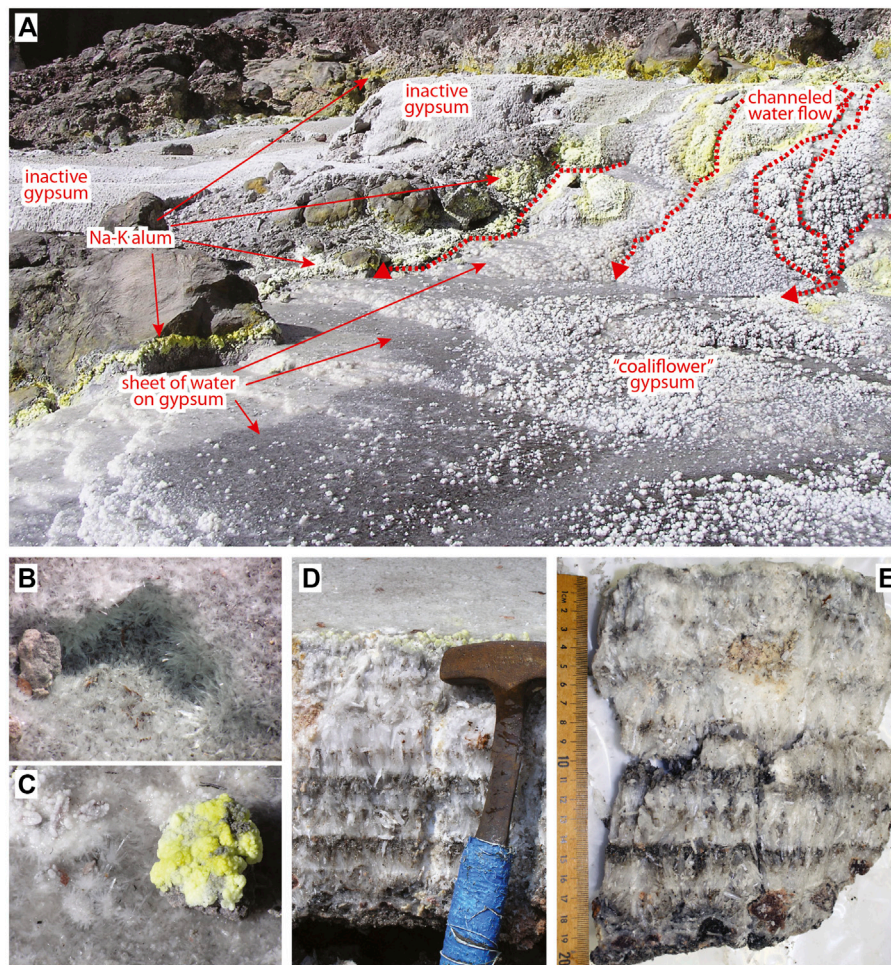
FIGURE 3 | (A–C) Types of gypsum found in the uppermost part of the plateau. Initial water flow is channelized and flows on sediment, with gypsum precipitation limited to a "cauliflower" type that extends above the water. The seepage water subsequently spreads out into a film on a sheet of flat-lying gypsum with mm-sized gypsum laths protruding upward into the fluid. Locally, ponds are present, with gypsum laths growing inward. Precipitation of yellow (Na-K)-alum is limited to the margins of the flow, and areas above the water level. **(D)**. View of the gypsum section (sample KV09-507L) before extraction, showing growth zoning outlined by dark debris horizons. The surface gypsum is covered with a film of water. **(E)**. The gypsum section as sampled.

is common on detritus including rock fragments and pieces of wood. Open caverns are present under a number of the steps. No water can be seen dripping from their gypsum roof, indicating that there is no permeability in the gypsum.

Cross-sections through the gypsum plateau show growth zoning (**Figures 3D,E**), outlined by both small color variations in the gypsum, and by horizons of detritus (mostly wood fragments, leaves, charcoal and variably altered rock fragments). These detritus horizons will reflect mud and debris flows onto the gypsum plateau. Growth zones are mostly horizontal and parallel to the upper gypsum surface, except where detritus is present and gypsum growth becomes radial (**Figure 3E**). Growth zones are remarkably regular, can be traced from one section to another, and are of near-constant thickness along a section. This suggests a spatially constant rate of growth.

Gypsum stalactites form on the overhangs of the steps (**Figure 2B** and Utami et al., 2019; Utami et al., 2020). These

stalactites have a conical shape, and where actively growing, they terminate in a transparent, idiomorphic gypsum lath that can be up to several cm in length. These laths were removed on a number of actively growing stalactites in 2008, and had completely regrown in 2009, indicating that they form rapidly. In cross-section, the stalactites show growth zoning, similarly outlined by gypsum color variations and detritus horizons (Utami et al., 2019).

The streamlets that feed the plateau are not fixed in location, nor is the water flow over the plateau itself. As a result, water meanders over the plateau and the water feed to a section of the plateau can shift from one spring to another. There are also sections of the plateau that are inactive (**Figure 2C**). The gypsum in these inactive parts is brittle and milky white to grey in color.

Gypsum is also found as fragments and grains in phreatic and phreato-magmatic deposits in the Banyu Pait river valley and on the outer flanks of the volcano, as gypsum needles cementing the

1817 base fall deposit (Utami et al., 2019), and as a surface coating on phreatic deposits around the crater. The latter appear to form from remobilization of SO_4 from the phreatic deposits, or from SO_4 formed in the oxidation of native sulfur contained within these deposits.

Gypsum precipitates are a long-lived feature of the Kawah Ijen system as evidenced by the presence of gypsum fragments in phreatic and phreato-magmatic deposits. Gypsum stalactites are mentioned in a report of an expedition to the crater lake and Banyu Pait River that took place in 1789 (Oudgast, 1820). A layer of gypsum just above the level of the lake is reported by Kemmerling (1921). However, neither author mentions the gypsum plateau, despite the fact that "Oudgast" (i.e., old-timer) descended along the river. Other authors describing the Kawah Ijen—Banyu Pait system in the late 19th and early 20th centuries also make no mention of the plateau, including Hengeveld (1920) who surveyed the upper river valley for the construction of a new dam and did observe the seepage springs that currently feed the plateau. Moreover, a photograph taken of the upper Banyu Pait river valley that shows the dam down to the plateau location during a spilling event around 1920 does not appear to show the gypsum plateau, although it is partly covered by water (**Figure 1C**). Combined, this suggests that a gypsum plateau was not yet present in the early 1920s, or at least not as significant as it is now.

Other precipitate phases found associated with the spring and river water include (Na,K)-alum, barite, syngenite, amorphous silica, and jarosite (Delmelle and Bernard, 2000; van Hinsberg et al., 2017; Utami et al., 2019).

METHODS AND MATERIALS

Layered gypsum was investigated as a timeseries of changes in the composition of the crater lake and hydrothermal effluent from which it formed, and thereby a proxy record for changes in volcanic input and activity. Absolute time was assigned to this record using noble gas corrected ^{210}Pb radionuclide dating. The gypsum record was converted to a fluid compositional record by use of partition coefficients.

Samples

Samples of the gypsum plateau were collected in 2009 from the central part of the plateau where active fluid flow occurs (**Figure 2B**). A 19 cm gypsum cross-section was cut that extends from the substrate to the actively growing surface (Sample KV09-507L). The surface of the gypsum consists of idiomorphic gypsum laths terminating on the fluid surface (**Figure 3D**). The gypsum cross-section consists of layered gypsum growing from a substrate of altered rock fragments (**Figures 3D,E**). Individual gypsum crystals can be recognized in the growth bands and consist of upward growing and broadening crystals that are transparent to milky white in color. Three distinct horizons of variably altered rock fragments are found in the cross-section, as well as isolated fragments of fresh and altered rocks, and organic material (twigs, leaves and charcoal). Radiating gypsum growth is

present where these foreign objects occur. Most of the layers are dense, but the gypsum immediately below the rock fragment horizons has porosity and is similar in texture to that of the actively growing surface, suggesting that it represents an active growth surface rapidly buried by influx of rock fragments.

A more detailed inspection of polished gypsum sub-samples from the transect sample was conducted by back-scattered electron microscopy and EDS semi-quantitative analysis using a PhenomXL SEM with CeB_6 electron source operating at 10 kV and Si-drift EDX detector. This imaging confirmed that the inclusions consist of variably altered magmatic rock fragments (containing glass, plagioclase, clino-pyroxene, Ti-magnetite and their altered equivalents—see Lowenstern et al., 2018; van Hinsberg et al., 2020) and organic debris, as well as euhedral to subhedral grains of barite, syngenite and (Na,K)-alum. The rock fragments and organic debris vary in size from ca. 100 μm to 3 cm, and are readily identifiable in the gypsum from their dark color. Barite, alum and syngenite range from submicron to minor larger grains of ~200 μm, with most approximately 2–10 μm. Whereas barite and syngenite are homogenously distributed, alum is commonly concentrated in bands.

To convert the gypsum composition to that of the fluid from which it formed requires knowledge of the partitioning of the elements between gypsum and fluid. To determine this, gypsum laths actively growing on gypsum stalactites were collected, as was the fluid from which these laths were growing. These laths had been broken off the year before sampling, so the laths that were sampled represent 1 year of growth. Three pairs of gypsum (KV08-407, KV09-505, KV09-303) and fluid (SP2008-L, KV09-506, KV09-304) were collected.

Gypsum and Fluid Compositional Analyses

The composition of gypsum was determined in-situ along a point transect using laser-ablation ICP-MS, and in bulk samples by wet ashing followed by solution ICP-MS. Bulk analyses were conducted on select growth bands in the gypsum cross-section that were further analyzed for ^{210}Pb and noble gases. Bulk analyses were also conducted on actively growing gypsum laths that were combined with fluid analyses to obtain partition coefficients. The growth bands represent clearly defined growth zones of sufficient width to yield the sample amounts needed for the combined analyses. The extracted gypsum growth zones were coarse crushed in an agate pestle and mortar, washed in ethanol to remove dust, and clear, inclusion-free crystals hand-picked with the help of a binocular microscope. An aliquot of ca. 250 mg was then finely ground in an agate mortar under ethanol and dissolved in 25 ml 10% trace element grade HNO_3 solution at 40°C under constant stirring. The resulting solutions were clear and devoid of precipitate/residue. Solutions were analyzed by ICP-QMS at GeoLabs (Sudbury, Canada). A sample of the outermost growth surface of the gypsum transect, consisting of mm-sized laths of gypsum that protrude from the surface and were submerged in the acid water when the sample was taken, was similarly crushed, washed in distilled water and ethanol to remove soluble co-precipitates (e.g., alum and syngenite) and dust, and finely ground in an agate mortar. The resulting powder

was pressed into a 13 mm diameter pellet without additives and analyzed by laser-ablation ICP-MS.

Laser-ablation ICP-MS analyses were conducted using a NewWave 213 nm Nd:YAG laser system coupled to a Thermo Finnigan iCAP Qc quadrupole ICP-MS in the trace-element laboratory of McGill University. The laser was operated at 10 Hz repetition rate, a 120 μm crater size and with a fluence of 5.5 J/cm^2 for the *in-situ* transect analyses. The pellet was sampled in troughs of ~10 mm length using a 20 Hz repetition rate, 80 μm crater diameter and fluence of 5 J/cm^2. In both types of analyses, the surface was cleaned prior to the analyses using a 140 μm crater. The ablated material was transported to the ICP-MS in an 800 ml/min He flow that was mixed with 1 L/min of Ar prior to injection into the ICP-MS plasma. NIST SRM 610 was used as the primary standard to correct for drift, and bracketed the gypsum analyses. Reference glasses BCR-2G, BIR-1G, KL2, and T1 were used as secondary standards to determine accuracy. Certified values for all SRM were the preferred values taken from the GEOREM database (Jochum et al., 2005). Calcium was used as the internal reference element to correct for variations in ablation behavior between gypsum and glasses, assuming a stoichiometric content of Ca in the gypsum. Data were processed using the Iolite version 2.5 software package (Paton et al., 2011). Each analysis spot was integrated in full (the full dataset) and integrated while excluding any obvious inclusions (the inclusion-filtered dataset). Inclusions were identified by inspecting the Ca-divided element signals, in particular Ba/Ca (barite), Al/Ca (alum), Mg/Ca (syngenite), and Si/Ca (silicates). The *in-situ* transect samples consisted of 2 cm long, polished sub-samples cut from the gypsum transect, and cover the full transect from base to top, except for some of the detritus horizons (**Supplementary Figure S1**). The laser ablation transect followed upward growing crystals and targeted the densest parts of the samples, and the transect is therefore kinked and discontinuous in places. The spacing between craters was varied, with the highest density, and hence resolution, for the most recent part of the transect. Analysis craters were located afterwards in optical microscopy (**Supplementary Figure S1**) and their position relative to the surface determined by projecting these positions onto the vertical.

The samples of the water from which the stalactite tips were growing were analyzed by ICP-OES for major elements and ICP-QMS for trace elements at GeoLabs (Sudbury, Canada). The digested samples were diluted 8 times in a trace element grade nitric acid solution for ICP-OES and 145 times for ICP-MS. Detection limits and reproducibility of reference materials for these methods are given in **Supplementary Table S1**.

^{210}Pb and Noble Gas Analyses

A *ca.* 1 g aliquot of the handpicked gypsum was ground under ethanol in an agate pestle and mortar and prepared for alpha spectrometry in the radionuclide laboratory at UQAM. The gypsum samples were dissolved in HCl spiked with a known mass of ^{209}Po tracer, plated onto silver discs, and the discs counted for Po isotopes using an EG&G Ortec 576 alpha spectrometer. Analyses followed the protocol of Utami et al.

(2019) and more details on the analytical method can be found there.

Noble gas He, Ne, Ar, Kr, and Xe concentrations and ^{40}Ar/^{36}Ar, ^{86}Kr/^{84}Kr, and ^{129}Xe/^{132}Xe ratios were determined at the Geotop GRAM laboratory at UQAM, by noble gas mass spectrometry (NGMS). Between 0.25 and 0.45 g of the material was hand-picked and placed in a stainless-steel vessel with a iron ball and pumped to vacuum overnight using a primary pump. Any washing, both in water and in ethanol/acetone was avoided, because previous essays showed that humidity is impossible to remove by pumping, likely because of the porosity and typology of the gypsum crystals. After a vacuum of less than 5×10^{-4} mbar was reached (measured on a Pirani gauge), the iron ball was agitated 200 times using an external magnet to crush the gypsum and release the noble gases for analysis. The reactive gases were removed using two Ti getters at 600°C for 15 min followed by 10 min at ambient temperature and one Zr-V-Fe SAES$^®$ ST-707 getter at 100°C for 15 min followed by 10 min at ambient temperature. Gases were then adsorbed onto an Advanced Research System$^®$ cryogenic trap containing activated charcoal at 11 K and released sequentially at 35 K (He), 110 K (Ne), 210 K (Ar), and 310 (Kr and Xe). Noble gas isotopes were measured using a Thermo$^®$ HELIX-MC using the axial Faraday detector in peak jumping mode. Signals were calibrated against a known aliquot of standard air. Typical air standard isotopic measurement reproducibility is 1.5–2%, while uncertainties on noble gas isotopic concentration analyses are between 0.1 and 0.01%.

The gypsum-fluid pair KV09-505 and KV09-506 was also analyzed for ^{210}Pb. The gypsum sample was treated as the transect gypsum growth zone samples described above. Approximately 20 g of the brine was accurately weighed into a glass beaker that contained a known mass of ^{209}Po yield tracer. The fluid was evaporated to dry and re-dissolved in 80 ml of 0.6 M HCl. Polonium isotopes were spontaneously deposited from this solution overnight onto silver disks and their activities counted in an EG&G Ortec 576 alpha spectrometer running the Maestro software. The gypsum and brine samples were measured 750 days after sampling to ensure equilibrium between ^{210}Po and ^{210}Pb.

RESULTS

Gypsum and Fluid Compositions

Table 1 presents the median and 1st and 3rd quartile gypsum compositions for the gypsum transect (full and inclusion-filtered integration windows for *in-situ* analyses and the GeoLabs bulk analyses) and the compositions of the gypsum-fluid pairs that were analyzed to obtain partition coefficients. The full datasets are given in **Supplementary Table S1**. Compared to the seepage waters, gypsum is particularly enriched in Sr, the LREE, Ni, Cu, Pb, and Mo, and depleted in the alkali elements, Be, Mg, Mn, Al, and the HFSE. The transect shows largest relative compositional variability in Zr, Ba, Tl, U, Sb, Ti, V, Mn, Nb, and Al.

The compositions of bulk-digested gypsum are equivalent to those measured *in-situ* (**Table 1**). There is more variability for the

TABLE 1 | Compositions of gypsum and fluid samples.

Sample	KV09-507L			KV09-507L			KV09-507L			KV09-303	KV09-304	KV09-505	KV09-506	KV08-407	SP08-L	KV09-507L	KV09-507L
Material	Gypsum			Gypsum			Gypsum			Gypsum	Fluid	Gypsum	Fluid	Gypsum	Fluid	Gypsum	Gypsum
Comment	Transect–full			Transect–inclusion filtered			Bulk digested samples			Stalactite tip	New spring	Stalactite tip	Main spring	Stalactite tip	Main spring	Top–pellet	Top–in-situ
	median	P25	P75	median	P25	P75	median	P25	P75								
Li	0.03	0.02	0.05	0.02	0.01	0.04	0.07	0.06	0.09	0.07	0.99	0.05	1.20	n.d.	0.59	0.25	0.07
Be	n.a.	n.a.	n.a.	n.a.	n.a.	n.a.	n.a.	n.a.	n.a.	n.d.	0.08	n.d.	0.09	n.d.	0.06	0.008	0.005
B	1.1	0.6	1.9	0.8	0.5	1.3	3.7	2.8	4.6	4.4	34.0	3.3	34.0	n.a.	n.d.	n.a.	n.a.
Na	62	31	104	40	20	76	92	84	112	79	1,025	123	1,130	n.a.	916	336	79
Mg	18	12	33	13	9	22	19	15	22	20	709	23	756	n.a.	567	43	19
Al	66	27	158	38	15	93	50	38	62	62	5,624	90	6,233	n.a.	4,772	329	1,572
Si	4,423	2,186	7,857	n.d.	n.d.	n.d.	8	6	10	n.a.	n.a.	n.a.	n.a.	n.a.	n.a.	n.a.	n.a.
K	27	13	54	18	7	35	55	44	59	52	1,206	56	1,354	n.a.	1,027	291	23
Ca	fixed	fixed	fixed	fixed	fixed	fixed	230,076	222,355	233,914	220,245	823	225,505	1,051	225,000	697	232,834	232,834
Sc	0.3	0.2	0.5	0.2	0.2	0.4	0.4	0.4	0.5	0.6	1.3	1.2	1.4	n.d.	1.1	1.0	0.4
Ti	1.5	0.6	4.1	0.8	0.4	2.1	0.9	0.8	1.0	1.0	36.5	1.0	25.9	12.9	20.3	34.0	3.6
V	0.15	0.07	0.35	0.08	0.04	0.21	0.09	0.07	0.11	0.14	12.32	0.18	13.38	0.13	10.78	2.36	0.84
Cr	n.a.	n.a.	n.a.	n.a.	n.a.	n.a.	0.11	0.09	0.12	0.13	0.82	0.08	0.44	0.01	0.28	0.34	0.35
Mn	0.7	0.3	1.6	0.4	0.2	0.9	0.4	0.3	0.4	0.5	48.1	0.6	51.1	0.6	42.2	7.2	1.0
Fe	n.a.	n.a.	n.a.	n.a.	n.a.	n.a.	18	15	26	32	2,567	37	2,617	n.a.	2,432	n.a.	n.a.
Co	0.11	0.09	0.12	0.10	0.09	0.12	0.81	0.76	0.85	0.81	0.59	0.91	0.61	0.34	0.61	0.27	0.19
Ni	1.4	1.3	1.4	1.3	1.3	1.4	0.7	0.6	1.1	0.8	0.2	1.0	0.2	n.a.	0.3	0.9	1.0
Cu	0.11	0.08	0.17	0.09	0.07	0.13	2.0	1.8	2.7	2.2	0.4	1.6	0.2	n.a.	0.1	1.5	0.2
Zn	0.3	0.2	0.5	0.2	0.1	0.4	14	4	63	2.8	6.1	26.9	6.2	6.0	n.d.	0.9	0.6
Ga	0.02	0.01	0.05	0.01	0.01	0.03	0.32	0.30	0.33	0.38	1.11	0.55	1.22	0.01	1.14	0.30	0.38
As	0.3	0.2	0.4	0.2	0.1	0.2	0.2	0.2	0.2	0.3	n.d.	0.3	n.d.	n.d.	n.d.	11.8	0.3
Rb	0.14	0.05	0.26	0.08	0.03	0.18	0.17	0.14	0.18	0.13	3.42	0.16	4.21	0.10	3.25	0.93	0.10
Sr	785	708	849	775	697	852	803	759	833	821	15	1,058	18	n.a.	14	888	852
Y	2.2	1.8	2.9	2.0	1.6	2.7	2.5	2.4	2.7	3.2	0.8	4.2	1.0	2.8	0.9	4.0	3.3
Zr	0.08	0.03	0.27	0.04	0.02	0.14	0.19	0.16	0.31	0.15	1.91	0.12	2.19	0.05	1.82	1.87	0.09
Nb	0.0012	0.0004	0.0038	0.0014	0.0007	0.0037	0.0016	0.0014	0.0019	0.0019	0.0019	n.d.	n.d.	n.d.	0.0008	0.058	0.0010
Mo	0.005	0.003	0.010	0.005	0.003	0.010	0.035	0.029	0.043	0.035	0.008	0.021	0.007	n.d.	n.d.	0.042	0.029
Cd	0.002	0.001	0.004	0.002	0.001	0.004	0.015	0.013	0.017	n.d.	0.036	n.d.	0.056	0.004	0.044	0.015	0.006
Sn	n.a.	n.a.	n.a.	n.a.	n.a.	n.a.	0.03	0.02	0.04	0.03	0.37	0.02	0.38	0.01	0.21	10.59	21.41
Sb	0.018	0.008	0.045	0.010	0.003	0.028	0.024	0.016	0.036	0.021	0.035	0.019	0.070	0.001	0.053	0.467	0.014
Cs	0.005	0.003	0.008	0.003	0.001	0.005	0.019	0.011	0.042	0.047	0.094	0.012	0.112	0.007	0.105	0.044	0.005
Ba	0.09	0.04	0.42	0.06	0.02	0.21	0.46	0.39	0.74	0.16	0.05	0.13	0.06	0.07	0.04	5.41	0.13
La	12	9	16	11	7	16	11	11	12	14	0.56	24	0.67	19	0.60	16	16
Ce	42	30	53	39	25	51	45	41	47	50	1.31	74	1.52	53	1.33	59	57
Pr	n.a.	n.a.	n.a.	n.a.	n.a.	n.a.	6.8	6.2	7.1	7	0.18	10	0.20	7	n.d.	8	8
Nd	28	19	35	26	18	35	29	27	30	32	0.76	40	0.87	31	0.73	36	38
Sm	4.6	3.4	5.7	4.4	3.0	5.6	4.9	4.6	5.1	5.5	0.18	6.8	0.20	4.9	0.16	6.4	6.6
Eu	1.0	0.8	1.2	0.9	0.7	1.2	1.0	0.9	1.0	1.2	0.05	1.4	0.06	1.0	0.05	1.5	1.3
Gd	2.0	1.6	2.4	1.9	1.5	2.4	2.2	2.1	2.3	2.7	0.17	3.4	0.19	3.9	0.17	3.0	2.8
Tb	n.a.	n.a.	n.a.	n.a.	n.a.	n.a.	0.23	0.22	0.23	0.3	0.03	0.4	0.03	0.3	0.03	0.4	0.3
Dy	n.a.	n.a.	n.a.	n.a.	n.a.	n.a.	0.99	0.96	1.02	1.3	0.16	1.6	0.18	1.0	0.15	1.5	1.3
Ho	n.a.	n.a.	n.a.	n.a.	n.a.	n.a.	0.13	0.13	0.14	0.2	0.03	0.2	0.04	0.1	0.03	0.2	0.2
Er	0.28	0.22	0.35	0.26	0.21	0.33	0.28	0.27	0.30	0.35	0.10	0.47	0.11	0.48	0.09	0.48	0.38

(Continued on following page)

TABLE 1 | (Continued) Compositions of gypsum and fluid samples.

Sample	KV09-507L			KV09-507L			KV09-507L			KV09-303	KV09-304	KV09-505	KV09-506	KV08-407	SP08-L	KV09-507L	KV09-507L
Material	Gypsum			Gypsum			Gypsum			Gypsum	Fluid	Gypsum	Fluid	Gypsum	Fluid	Gypsum	Gypsum
Comment	Transect-full			Transect-inclusion filtered			Bulk digested samples			Stalactite tip	New spring	Stalactite tip	Main spring	Stalactite tip	Main spring	Top-pellet	Top-in-situ
	median	P25	P75	median	P25	P75	median	P25	P75								
Tm	n.a.	n.a.	n.a.	n.a.	n.a.	n.a.	0.03	0.03	0.03	0.03	0.01	0.04	0.02	n.a.	n.d.	0.06	0.03
Yb	0.13	0.10	0.16	0.12	0.09	0.15	0.12	0.12	0.13	0.15	0.09	0.20	0.10	0.19	0.09	0.27	0.17
Lu	n.a.	n.a.	n.a.	n.a.	n.a.	n.a.	0.01	0.01	0.01	0.02	0.01	0.02	0.02	0.02	0.01	0.05	0.02
Hf	n.a.	n.a.	n.a.	n.a.	n.a.	n.a.	0.01	0.01	0.01	0.011	0.037	0.015	0.043	0.010	0.036	0.059	0.001
Ta	0.0002	0.0001	0.0004	0.0003	0.0001	0.0005	0.0008	0.0006	0.0010	0.0004	n.d.	0.0005	n.d.	n.a.	0.0001	0.0051	0.0001
W	0.004	0.002	0.008	0.003	0.001	0.006	0.016	0.012	0.020	0.020	n.d.	0.014	0.002	0.009	n.a.	0.249	0.123
Tl	0.054	0.038	0.077	0.015	0.006	0.042	0.042	0.035	0.045	0.031	0.635	0.043	0.721	0.058	0.702	0.186	0.053
Pb	17.2	14.2	19.3	15.8	12.2	18.5	16.3	15.3	17.5	16.4	3.4	24.0	4.1	24.2	3.9	19.0	15.9
Bi	0.19	0.11	0.27	0.18	0.08	0.25	0.19	0.16	0.21	0.31	0.62	0.20	0.66	n.a.	0.71	0.43	0.13
Th	0.25	0.16	0.36	0.22	0.14	0.32	0.28	0.27	0.30	0.39	0.25	0.71	0.28	0.45	0.25	0.88	0.50
U	0.0017	0.0007	0.0044	0.0010	0.0004	0.0028	0.0014	0.0010	0.0022	0.002	0.055	0.002	0.061	0.004	0.051	0.091	0.022

Concentrations for the gypsum transect (both the full and inclusion-filtered integration windows), and bulk digested gypsum are given as the median and 1st and 3rd quartile. The full dataset of in-situ gypsum analyses is given in **Supplementary Table S1**. All values are given in mg/kg.

in-situ analyses, which is to be expected as the bulk analyses represent a larger growth interval and will therefore average out the variability. The Cu, Co, and Zn contents of the bulk-digested samples are consistently higher. It is unclear what causes this as no inclusion phase with these specific elements was identified in electron imaging. The equivalence in composition between *in-situ* and bulk analyses indicates that the bulk analyses are representative of gypsum, as there is no evidence for a significant presence of inclusions in the bulk-digested samples. For example, the median Al content of the bulk-digested gypsum is 50^{+12}_{-12} mg/kg and it is 38^{+55}_{-23} mg/kg for the *in-situ*, inclusion-filtered analyses, which rules out a significant presence of alum. Similarly, Si contents are low at a median of only 8 ± 2 mg/kg. This means that the ^{210}Pb activities and noble gas data determined from bulk samples are representative for gypsum.

Noble Gas and ^{210}Pb Data

The noble gas data are given in **Table 2**, and the ^{210}Pb activities for these same growth horizons in **Table 3**. The ^{210}Pb data for the gypsum-fluid pairs are given in **Table 4**.

The gypsum samples contain minor amounts of ^{4}He and ^{22}Ne (a few fA signal on the Faradays axial cup of the HELIX-MC mass spectrometer), which precluded the precise measurement of their isotopic composition (i.e., ^{3}He/^{4}He, ^{20}Ne/^{22}Ne, and ^{21}Ne/^{22}Ne), whereas Ar, Kr, and Xe concentrations were high, which enabled us to obtain precise isotopic ratios (100–1,000 fA signal on axial Faraday' cup). The abundance ratios ^{4}He/^{36}Ar, ^{20}Ne/^{36}Ar, ^{87}Kr/^{36}Ar, and ^{132}Xe/^{36}Ar, normalized to the same ratios in the atmosphere for simplicity (the so-called F-values: $(^iX/^{36}Ar)_{sample}/(^iX/^{36}Ar)_{air}$) show values from near atmospheric for Ne/Ar (0.97–4.79), to ratios of 90–2000 for Kr/Ar and Xe/Ar indicating a contemporary enrichment for the lighter and heavier noble gases compared to the atmosphere in the gypsum. A similar observation was reported for gypsum by Utami et al. (2019).

The observed enrichments are not unique in geological materials and have been observed in several environments, with F-Xe enrichments ranging from 10 to 10,000 (e.g., Torgersen et al., 2004). Enrichments are reported for sedimentary rocks (oceanic sediments—Matsuda and Nagao 1986; Pitre and Pinti 2010 and shales—Fanale and Cannon 1971; Bernatowicz et al., 1984); tephra (Pinti et al., 1999); and hydrothermal deposits (geothermal amorphous silica—Matsubara and Matsuda 1988 and hydrothermal quartz—Fairmaid et al., 2011). F-values measured in the Kawah Ijen gypsum overlap with shales and amorphous silica (**Supplementary Figure S2**) and there is a near perfect match for F-Kr and F-Xe with amorphous silica precipitated in geothermal areas, which represent the closest depositional environment to that where Kawah Ijen gypsum precipitated.

The ^{40}Ar/^{36}Ar ratios range from a likely atmospheric but mass-fractionated value of 290.0 ± 0.9 (air $= 295.5$; Ozima and Podosek, 1983) up to a value of 316.1 ± 1.1 (**Table 2**). The ^{86}Kr/^{84}Kr ratios range from 0.2974 ± 0.0022 to 0.31255 ± 0.00042, close to the atmospheric value of 0.30524 (Ozima and Podosek, 1983) with some mass-fractionation. The ^{129}Xe/^{132}Xe ratios vary between 0.9193 ± 0.0029 and 1.0245 ± 0.0054, with the

TABLE 2 | Noble gas data for growth horizons in the gypsum section (KV09-507) and the 1-year gypsum growth (KV09-503).

Sample no.	^{4}He	1s	^{22}Ne	1s	^{36}Ar	1s	^{84}Kr	1s	^{132}Xe	1s
	• 10^{-8}		• 10^{-9}		• 10^{-8}		• 10^{-9}		• 10^{-10}	
KV09-507L-C	1.578	0.001	2.27	0.02	2.89	0.01	1.34	0.03	5.1	0.1
KV09-507L-D	0.570	0.001	1.54	0.01	1.817	0.008	5.0	0.2	52	1
KV09-507L-E1	0.321	0.005	0.63	0.02	0.354	0.001	0.339	0.002	0.80	0.02
KV09-507L-E2	0.5303	0.0005	1.4	0.2	2.43	0.02	2.7	0.1	5.9	0.2
KV09-507L-F	1.157	0.002	1.87	0.02	0.730	0.004	13.7	0.2	39.1	0.8
KV09-507L-G1	0.307	0.001	0.70	0.02	0.329	0.003	4.80	0.09	20.0	0.4
KV09-507L-G2	0.4888	0.0004	0.59	0.01	0.290	0.001	0.8	0.1	8.4	0.1
KV09-507L-H1	0.2450	0.0004	0.51	0.01	0.884	0.008	3.70	0.07	5.6	0.2
KV09-507L-H2	0.413	0.008	0.42	0.02	0.316	0.001	1.93	0.05	48.2	0.8
KV09-503	6.963	0.004	0.36	0.01	0.685	0.007	3.2	0.1	10.70	0.02

Sample no.	^{40}Ar/^{36}Ar	1s	^{86}Kr/^{84}Kr	1s	^{129}Xe/^{132}Xe	1s
KV09-507L-C	290.0	0.9	0.3096	0.0006	0.928	0.017
KV09-507L-D	304.9	0.9	0.3111	0.0003	0.919	0.003
KV09-507L-E1	295.1	0.7	0.297	0.002	0.99	0.04
KV09-507L-E2	297.1	0.8	0.3131	0.0004	0.974	0.008
KV09-507L-F	304	1	0.2998	0.0007	0.983	0.006
KV09-507L-G1	315	1	0.3083	0.0004	1.017	0.007
KV09-507L-G2	308	1	0.3150	0.0005	0.960	0.004
KV09-507L-H1	315	1	0.3049	0.0007	0.98	0.02
KV09-507L-H2	304.7	0.8	0.3117	0.0007	0.981	0.005
KV09-503	316	1	0.3126	0.0004	1.025	0.005

Growth zone C is stratigraphically the youngest, and H2 the oldest. Concentrations are reported as ccSTP/g and their 1 standard deviation uncertainty.

TABLE 3 | ^{210}Pb data for growth horizons in the gypsum section (KV09-507) and the 1-year growth (KV09-503), and the noble gas corrected apparent ages for these samples. Not analysed—n.a.

Sample no.	^{84}Kr/^{36}Ar	1s	^{132}Xe/^{36}Ar	1s	k Kr	k Xe	Wt. k	^{210}Pb	1s	Age	1s
507L-C	0.046	0.001	0.018	0.001	0.10	0.11	0.10	0.59	0.02	-49	4
507L-D	0.27	0.01	0.285	0.006	0.59	1.83	1.04	0.63	0.02	24	2
507L-E1	0.096	0.001	0.023	0.001	0.21	0.15	0.17	0.36	0.01	-16	1
507L-E2	0.113	0.004	0.024	0.001	0.24	0.15	0.23	0.34	0.00	-4.6	0.4
507L-F	1.88	0.03	0.54	0.01	4.02	3.43	3.85	0.47	0.02	77	6
507L-G1	1.46	0.03	0.61	0.01	3.13	3.89	3.38	n.a.	-	-	
507L-G2	0.27	0.05	0.290	0.005	0.58	1.86	0.70	0.53	0.02	17	3
507L-H1	0.419	0.009	0.064	0.003	0.90	0.41	0.78	0.52	0.02	21	2
507L-H2	0.61	0.02	1.52	0.03	1.31	9.75	6.40	0.46	0.02	94	7
KV09-503	0.47	0.02	0.156	0.002	1	1	1	0.91	0.03	11	-

Uncertainties are reported as 1 standard deviation and ^{210}Pb values are given in decays per minute per Gram of gypsum (dpm/g).

atmospheric value being 0.9832 (Ozima and Podosek, 1983). Interestingly there is no relationship between ^{86}Kr/^{84}Kr and ^{40}Ar/^{36}Ar ratios, indicating that high ^{40}Ar/^{36}Ar values are not caused by mass-fractionated atmospheric Ar diffusing from the sample, as observed in some tephra (Pinti et al., 1999), but rather reflects addition of terrigenic (crustal and/or mantle) ^{40}Ar*. Given the very young age of the samples, their low K content (a few tens of ppm; **Table 1**) and the absence of detrital components in the crushed crystals, ^{40}Ar/^{36}Ar ratios higher than the atmosphere cannot be related to *in situ* production of radiogenic ^{40}Ar*, but only associated with the addition of mantle Ar. Interestingly, there is a positive trend between ^{40}Ar/^{36}Ar and ^{129}Xe/^{132}Xe (not shown here), possibly suggesting a small anomaly in mantle ^{129}Xe (Staudacher and Allègre, 1982), to be confirmed by further analyses.

TABLE 4 | ^{210}Pb data for gypsum—fluid pairs and the tip laths of stalactites.

Sample no.	Type	^{210}Pb	1s
KV09-505	Stalactite tip	1.50	0.05
KV09-506	Fluid	0.247	0.009
KV09-501	Stalactite tip	1.33	0.05
KV09-503new	Stalactite tip	1.28	0.05
KV08-407	Stalactite tip	1.16	0.09

Values are given in dpm/g with their 1 s uncertainty and have been recalculated for their ^{210}Pb activity at the time of sampling.

Gypsum-Fluid Element Partition Coefficients

Partition coefficients for the natural gypsum-fluid pairs are shown in **Figure 4A** where $D_i = C_i^{gypsum}/C_i^{fluid}$, and i is the

element of interest and C is its concentration in mg/kg. Results for the different pairs are consistent in inter-element trends, but do show a spread in absolute values of, commonly, up to 1 log unit. In part, this spread results from analytical uncertainty, in particular where the element is close to the detection limit in one of the sample materials (e.g., Rb in gypsum), but for others, it may reflect the presence of micro-inclusions in the gypsum (e.g., Ba, Hf, and Al). The median value for each element was chosen as the representative partition coefficient, and is shown with an emphasized symbol in **Figure 4A**.

Strontium, Ni, Cu, Ba, Pb, Mo, and the REE are compatible in gypsum, whereas the alkalis, Tl, Mg, Zn, Mn, Cd, B, Al, and the HFSE are incompatible. This element association agrees with that which would be expected from the charge and size of the cation site in the gypsum structure. The REE + Sc + Y illustrate this particularly well when their D values are plotted against their ionic radii (Shannon, 1976) in an Onuma diagram (Onuma et al., 1968). A Lattice-Strain Theory fit (Blundy and Wood, 1994) through these data (**Figure 4B**) provides an estimate of 1.118 Å (111.8 pm) for the ideal radius, which is equivalent to that of Ca^{2+} in cubic coordination (1.12 Å, 112 pm).

The partition coefficients reported here are apparent partition coefficients, because it is not known whether gypsum grew in full equilibrium with the fluid. Gypsum precipitates because the fluid reaches gypsum supersaturation by evaporation and cooling (Delmelle and Bernard, 2000; Utami et al., 2019) and non-equilibrium element partitioning can develop under such conditions. In general, elements do not reach the equilibrium and maximum fractionation between mineral and fluid under non-equilibrium conditions, resulting in D-values that are closer to unity than at equilibrium. There are no experimentally-determined D-values for gypsum, as far as we are aware, and the gypsum-fluid D-values reported by Inguaggiato et al. (2020) for gypsum precipitated from vials containing Kawah Ijen lake waters represent bulk solids that include co-precipitated barite, Al-sulfates as well as a silicate (likely amorphous silica). The major element composition of these bulk solids, in particular their high Na and K contents (**Table 3** of Inguaggiato et al., 2020), suggests that these co-precipitated phases contribute significantly to the bulk composition. The REE are not expected to be compatible in these co-precipitated phases (cf. the D_{REE} for alum in **Figure 4B**), and the bulk digestion method would thus dilute the overall REE content, leading to lower apparent gypsum D_{REE}. The trend in the D_{REE} is, however, consistent with what we observe.

Assuming that the present-day formation conditions for gypsum are equivalent to those in the recent past, the apparent partition coefficients determined here can be applied to reconstruct fluid concentrations along the plateau transect. It can, nonetheless, not be excluded that some of the variability observed results from changes in D-values.

The partition coefficient for ^{210}Pb is the same as that of Pb within their respective 1s uncertainties (5.88 ± 0.24 for Pb and 6.07 ± 0.22 for ^{210}Pb). This indicates that ^{210}Pb is incorporated into gypsum as Pb, and is not the ingrowth product from incorporation of parent isotope Rn. Lead is also compatible in (Na,K)-alum and, especially in barite (**Figure 4A**). Assuming that

[210]Pb is similarly incorporated as Pb in these phases, a significant fraction of the ^{210}Pb could potentially be hosted by these inclusion phases. However, the low Al content of the bulk-digested samples shows that alum can only be a minor component in the bulk digestion solution that was analyzed for ^{210}Pb, and the use of a 40°C HCl digestion solution in preparing the samples for ^{210}Pb analysis should have prevented barite from dissolving. There is therefore no evidence that the ^{210}Pb contents are affected by barite, alum or other possible inclusion phases.

## [210]Pb Timeseries and Mass Balance

The ^{210}Pb activity timeseries does not show a progressive decrease in ^{210}Pb with stratigraphic position (i.e., time), which would be expected if decay were the only variable controlling the ^{210}Pb activity (**Figure 5**; cf. Ali et al., 2008). This behavior can reflect diffusional mobility of Pb in gypsum, a non-constant initial ^{210}Pb activity, or variable ingrowth because of differences in the parent-isotope concentrations. The latter can be discounted, because the activity of [226]Ra, the main parent isotope of sufficient longevity, is negligible (*ca.* 0.003 dpm/g as determined from preliminary γ-counting on Kawah Ijen gypsum samples). There appear to be no data on volume diffusion of elements in gypsum, but rapid variations in Li content along the transect (**Supplementary Figure S4**) suggest diffusion to be slow, given that Li is one of the fastest diffusing elements in minerals owing to its small ionic radius and 1 + charge (cf. Brady and Cherniak 2010). Variations among the growth zones in the starting ^{210}Pb content at time of formation is therefore the likely cause for the irregular [210]Pb *vs.* time. This cause was also argued by Utami et al. (2019) for gypsum stalactites at Kawah Ijen, and tied to variations in the volcanic flux of parent isotope [222]Rn.

Seepage water ^{210}Pb has two main sources: **1.** Rock leaching, which is the principal source of cations to the lake; and 2. Volcanic gas, which predominantly contributes anions and volatile (semi-)metals (van Hinsberg et al., 2017). Rock leaching is thought to involve mostly material falling into the lake in rock falls and slides, which are common, and therefore primarily includes magmatic deposits exposed in the crater walls (van Hinsberg et al., 2010b, 2017). These are predominantly basalts and basaltic-andesites, with lesser andesite and dacite. The ^{210}Pb in these magmatic deposits ultimately derives from the decay of [238]U, along a series of intermediate isotopes with variable half-lifes. In a first approximation, we assume the U decay series to be in secular equilibrium, in which case the activities of all isotopes of the decay series are equal. This permits calculating the ^{210}Pb content from the U concentration of the bulk rocks. Using the mean U contents of Kawah Ijen basalt, andesite and dacite (0.67, 2.3, and 3.5 mg/kg, respectively–van Hinsberg et al., 2010b), the ^{210}Pb activity of these rocks is 0.5, 1.7, and 2.6 dpm/g of rock. Kawah Ijen lake water reflects 42 ± 2 g of rock leaching per kg of water (van Hinsberg et al., 2010b), meaning that leaching would contribute between 0.02 (basalt) and 0.11 (dacite) dpm of ^{210}Pb per g of lake water. This is significantly lower than the measured ^{210}Pb activity in seepage waters of 0.25 dpm/g water (**Table 4**). Moreover, common Pb is retained during leaching by incorporation into the secondary
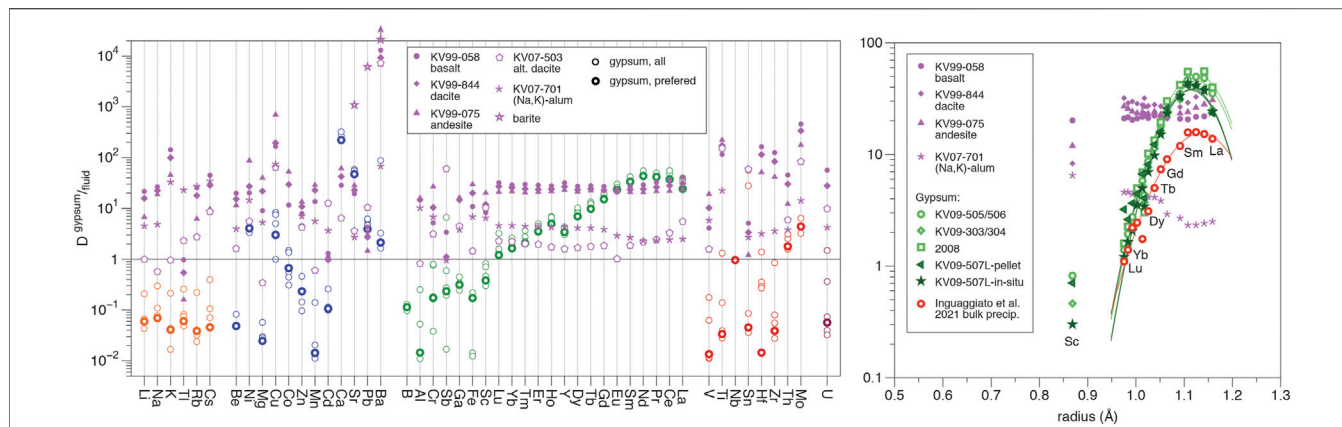
FIGURE 4 | (A). Gypsum-fluid element partition coefficients as determined from co-sampled pairs of actively growing gypsum and the fluid from which it was growing. Element are ordered by charge and then increasing radius. The apparent fluid partition coefficients for Kawah Ijen magmatic deposits, their altered equivalent (Na,K)-alum and barite are shown for comparison. The LREE and Sr are strongly compatible in gypsum, whereas the alkalis and HFSE are incompatible. **(B)**. Onuma diagram for the 3 + elements and Lattice-Strain Theory (LST) fits through these data for gypsum (solid lines). Adherence to LST indicates that element incorporation is controlled by the crystallography of the gypsum mineral structure. The ideal radius derived from the LST fit (1.118 Å) corresponds to that of Ca^{2+} in cubic coordination (1.12 Å), showing that the REE reside in the Ca site. The gypsum D-values presented here are higher than those of Inguaggiato et al. (2020), likely because of dilution of the gypsum REE content by the presence of other phases in the bulk-digested precipitate.
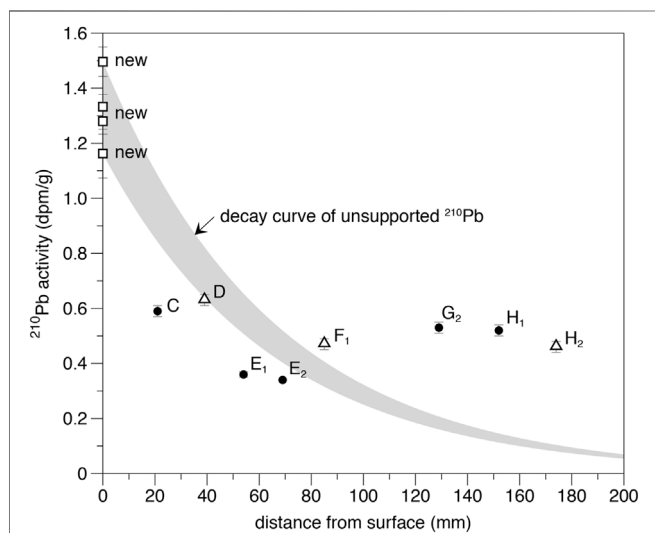
FIGURE 5 | Activity of ^{210}Pb for the growth zones versus their stratigraphic position in the transect. A simple unsupported ^{210}Pb decay curve cannot explain the observed trend as ^{210}Pb activity does not consistently decrease with distance. The uncertainty shown is 1 standard deviation.

phase barite, with a 10-fold reduction in the Pb leaching flux (van Hinsberg et al., 2010b). All isotopes of Pb should show equivalent behavior, and the total ^{210}Pb contribution from leaching can thus be expected to be only 0.002 to 0.011 dpm/g fluid. This dissolved element load of the lake has built up progressively, and concurrent ^{210}Pb decay must therefore be taken into account. Using the lake water total dissolved solids timeseries (**Figure 5** in van Hinsberg et al., 2017) as the leaching flux, we calculate a maximum rock contribution of 0.002 dpm/g at ~1900, with decay exceeding input of ^{210}Pb thereafter. This indicates that rock leaching can only be a minor contributor to the ^{210}Pb activity of the seepage waters and volcanic gas must be the main source.

Volcanic gas is an important source for "excess" ^{210}Pb in volcanic systems, because parent isotope ^{222}Rn is a gas, and is mobilized in volcanic degassing (see Berlo and Turner 2010 for a review). Vigorous gas injection into the lake was observed by Takano et al. (2004) in echo-soundings of the lake, and is further evident from bubbling of lake waters at the dam and fumaroles. Measurements of volcanic gas Rn activity show it to be high; 1.2—2.3 • 10^5 dpm/m^3 for Etna fumaroles (Giammanco et al., 2007) and 2.4—9.0 • 10^5 dpm/m^3 for 500°C Merapi fumaroles (Zimmer and Erzinger 2003). Volcanic gas is thus a viable source for the ^{210}Pb in the lake waters, and fluctuations in this volcanic flux (Merapi fumaroles varied from 2.4 to 8.4 • 10^5 dpm/m^3 within a single day—Zimmer and Erzinger 2003) will lead to variations in the ^{210}Pb$_0$ in the seepage waters from which the gypsum grew.
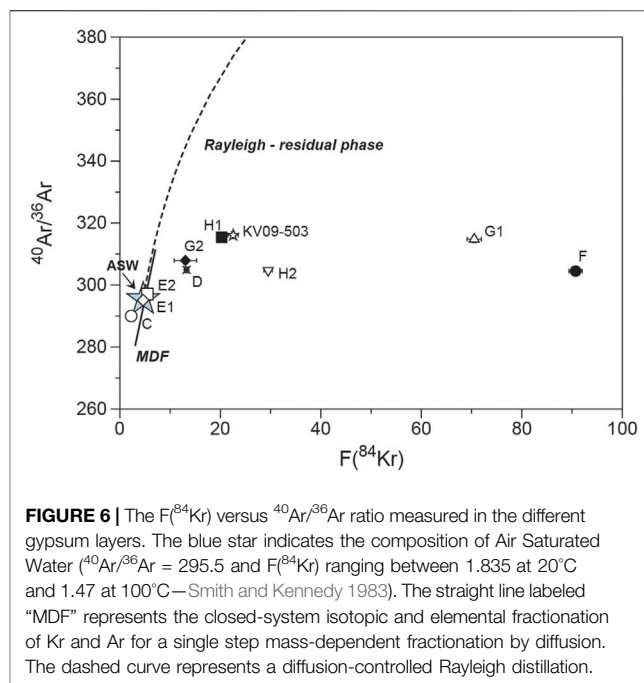
Absolute Age Assignment

The half-life of Rn is only 3.8 days and variations in the Rn-flux are only preserved in Rn activity for a few weeks. A different recorder of variations in Rn-flux is thus required to correct for the resulting changes in ^{210}Pb$_0$. Concentrations of Rn are insufficient for it to form its own gas phase. Rather, it partition into any gas phase formed by the major volatiles CO_2 and H_2O, as do other minor volatile components including the other noble gases. We previously proposed a correction method based on the content of the stable isotopes of the noble gases Kr and Xe in gypsum as a proxy for the volcanic gas flux (Utami et al., 2019). We chose Kr and Xe, because, as noble gases, their elemental behavior will be similar to Rn, and their isotopic composition allows for source identification. The noble gases are assumed to be dominantly present in fluid inclusions in the gypsum, trapped at time of growth, and therefore to reflect the noble gas composition of the formation fluid.

Noble gases in the gypsum formation waters are dominantly sourced from atmosphere, either directly or via an air-saturated groundwater intermediary, and from the magmatic-hydrothermal system. The noble gas contribution from rock leaching can be expected to be negligible. The elemental ratios of the noble gases measured in the gypsum samples are elevated compared to the atmosphere, with large anomalies in the F-values of Kr and Xe (**Supplementary Figure S2**). The mass dependence in the F-values for gypsum is common and has also been reported for sedimentary, volcanic, and hydrothermal deposits (e.g., Fanale and Cannon 1971; Bernatowicz et al., 1984; Matsuda and Nagao 1986; Matsubara and Matsuda 1988; Pinti et al., 1999; Pitre and Pinti 2010; Fairmaid et al., 2011). The current consensus hypothesis (Torgersen et al., 2004) is that this predominantly reflects diffusion-control, with retention of the heavier, larger-size Kr and Xe compared to Ar, Ne, and He. The gypsum noble gas composition could thus result from atmospheric noble gases diffusing in and out of the sample at different rates. However, when this process is modeled in $F(^{84}Kr)$ vs the $^{40}Ar/^{36}Ar$ space for single step mass-dependent fractionation in a closed system (see e.g. Kaneoka 1994), or for an open-system diffusion-controlled Rayleigh distillation, the gypsum data do not follow the resulting trends (**Figure 6**). Rather, the gypsum samples define a trend from the atmospheric reservoir (Air Saturated Water) to a component with magmatic $^{40}Ar^{\star}$ excesses and high Kr/Ar and Xe/Ar ratios, which we interpret to be the magmatic-hydrothermal system. The preservation of magmatic Ar in a volcano-sedimentary deposit such as gypsum could appear odd, but Cogliati et al. (2021) have recently shown mantle $^{40}Ar^{\star}$ excess preserved in even more fragile volcanic eruptive products such as Pele's hairs and tears, indicating that magmatic Ar can be retained in a variety of volcanic products that were previously not considered as a reliable magmatic record, due to their propensity for being contaminated by air.

Having established that the noble gas signature of gypsum reflects binary mixing of atmosphere and a volcanic component, we can quantify the variations in the relative volcanic contribution, which we equate to variations in the volcanic Rn-flux. We use ^{84}Kr and ^{132}Xe as two independent measures of the volcanic contribution, normalized to ^{36}Ar to correct for differences in the absolute amount of noble gas recovered from each sample. The weighted mean of $^{84}Kr/^{36}Ar$ and $^{132}Xe/^{36}Ar$ is then normalized to these same ratios for a gypsum sample of known age as the time anchor point. For $^{84}Kr/^{36}Ar$, following Utami et al. (2019):

$$^{84}Kr/^{36}Ar\,(Gypsum) = x \cdot {}^{84}Kr/^{36}Ar\,(Atmosphere) + (1 - x)$$
$$\cdot {}^{84}Kr/^{36}Ar\,(Volcanic\,gas)$$

A higher mass fraction of volcanic gas would reflect a higher ^{222}Rn flux, and hence a higher $^{210}Pb_0$, and we assume that this relationship is linear in a first approximation. This allows us to calculate the $^{210}Pb_0$ for the various growth zones relative to the $^{210}Pb_0$ for the sample of known age (where the ^{210}Pb initial for the known-age sample can be calculated from the measured ^{210}Pb and

FIGURE 6 | The $F(^{84}Kr)$ versus $^{40}Ar/^{36}Ar$ ratio measured in the different gypsum layers. The blue star indicates the composition of Air Saturated Water ($^{40}Ar/^{36}Ar$ = 295.5 and $F(^{84}Kr)$ ranging between 1.835 at 20°C and 1.47 at 100°C—Smith and Kennedy 1983). The straight line labeled "MDF" represents the closed-system isotopic and elemental fractionation of Kr and Ar for a single step mass-dependent fractionation by diffusion. The dashed curve represents a diffusion-controlled Rayleigh distillation.

its age at time of measurement): $^{210}Pb_0^{growth\,zone} = {}^{210}Pb_0^{growth\,zone}k$, where k is the uncertainty-weighted mean of k_{Kr} and k_{Xe} and

$$k_{Kr} = \frac{^{84}Kr}{^{36}Ar}\,(growth\,zone)/\frac{^{84}Kr}{^{36}Ar}(known\,age),$$
$$k_{Xe} = \frac{^{132}Xe}{^{36}Ar}\,(growth\,zone)/\frac{^{132}Xe}{^{36}Ar}(known\,age)$$

The sample of known age in these calculations is sample KV09-503 (this is a different sample than that used by Utami et al., 2019, and was a tip growing on a stalactite in close proximity to the gypsum plateau sample site from the same water flow).

Variations in the volcanic gas flux are potentially also recorded by other elements, in particular the volatile metals, which are enriched in the gas emissions at Kawah Ijen (van Hinsberg et al., 2017). This would permit a higher resolution age determination, as less sample material is required for elemental than noble gas analyses. We therefore compared the noble gas compositions for the investigated samples to the concentrations of all elements determined for these same samples by bulk-digested ICP-OES and ICP-MS, but found no statistically significant correlations with any of the elements. Similarly, dividing the ^{210}Pb activities by the volatile (semi-)metals does not produce a stratigraphy-consistent ^{210}Pb decay pattern. This indicates that the elemental compositions can, unfortunately, not be used to correct for variations in volcanic gas flux, not even those elements that are enriched in the fumarole emissions. This is probably because these elements are still derived from multiple sources, and although they are enriched in the gaseous emissions, they are not sufficiently exclusive to the gas to be used as a monitor of volcanic gas flux. The measurements of $^{40}Ar/^{36}Ar$ higher than the atmospheric value (**Table 2**), a first in

hydrothermal gypsum, corroborate that noble gases are recording the active volcanic flux through the Kawah Ijen system.

The noble gas corrected ^{210}Pb data define two parallel, age-consistent trends in a plot versus stratigraphic distance (**Figure 7**), both trends defining a growth rate of 2 mm/year. The offset between these two linear trends is best explained by the sample of known age not reflecting the source fluid for the full duration of growth of the plateau. The gypsum plateau is fed by a number of seepage springs, some of which coalesce, whereas others feed only a restricted part of the plateau (**Figures 2**, **3**), and flow patterns have likely changed over time. The various springs differ in their composition, although elemental ratios are similar, suggesting that the variations are mainly the result of different degrees of dilution by circumneutral groundwater. The ^{210}Pb activity of gypsum needles grown from various streamlets also varies (**Tables 3**, **4**), confirming that the fluid ^{210}Pb$_0$ activity is variable. The two trends are thus interpreted to reflect growth from two distinct fluid sources with variable ^{210}Pb$_0$ and/or noble gas contents, but both define a common, and constant upwards gypsum growth rate of 2 mm/year. This constant growth rate suggests that a dynamic equilibrium has established itself between the residence time of seepage fluids on the plateau surfaces and saturation of these fluids in gypsum by cooling and evaporation. This is supported by the apparent spatially constant growth rate as evidenced by growth layers of constant thickness along plateau cross-sections (see also 2.2). The 2 mm/year rate has been used to assign absolute ages to the growth zones in the plateau transect.

DISCUSSION

The integrity of the gypsum record depends on gypsum capturing a characteristic and reproducible fingerprint of the fluid composition, and for this fingerprint to be preserved. This requires constant partition coefficients for elements between gypsum and fluid, continuity in growth, and a lack of post-formation element mobility. Given that the seepage fluids are not saturated in gypsum where they emerge, and reach saturation only by cooling and evaporative concentration, gypsum formation is likely affected by weather conditions, with most precipitation expected when evaporation is most pronounced. As a result, growth is unlikely to be continuous throughout the year, and biased towards the dry season. Moreover, fluid dilution by rainfall would lead to undersaturation, and potential dissolution of gypsum. Indeed, a full day of undersaturation would be predicted to dissolve 0.2 mm of gypsum as calculated from the experimentally-determined dissolution rate data of Zaier et al. (2020) for low-porosity, crystalline gypsum. With 176 rainy days per year and a total precipitation of 2,416 mm/year at the nearby city of Banyuwangi (data from www.climate-data.org), dissolution should be an important process. Indeed, the surface layer of the crater lake is strongly diluted during the rainy season (Sumarti, 1998). Nonetheless, the very presence of the plateau, and its persistent growth as identified from visible growth zoning and quantified in the age model, indicate that growth exceeds dissolution, or that dissolution is kinetically limited.
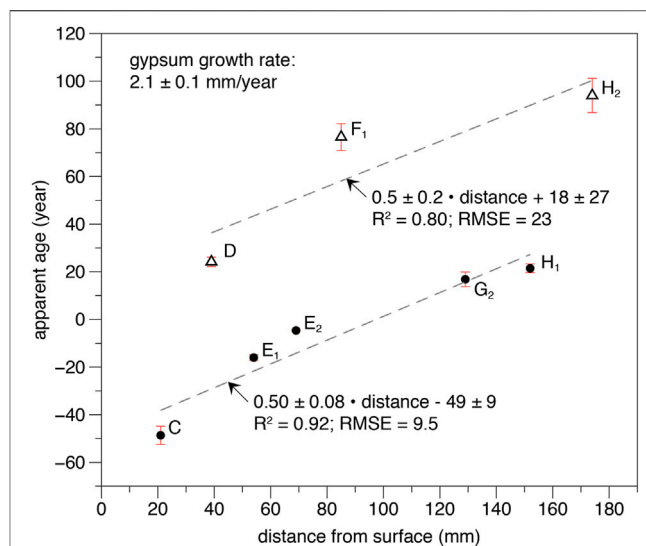
FIGURE 7 | Apparent ages for the gypsum growth zones based on ^{210}Pb activities corrected for variations in volcanic Rn-flux with noble gases. The ages define two parallel trends with equivalent slopes of 2 mm of gypsum growth per year. The two trends are interpreted to represent growth from two seepage flows. Uncertainties are 1 standard deviation.

Repeated mineral precipitation and dissolution can lead to a progressive increase in compatible elements, and removal of incompatible elements (*cf.* zone refining (Pfann, 1962). A negative correlation between compatible and incompatible elements would in this case develop, assuming variable precipitation-dissolution throughout the gypsum transect. Plotting Ce/Sr versus Ti/Sr or Sc/Sr, where Ce is compatible and Ti and Sc are incompatible, does not show the expected negative correlation (**Supplementary Figure S3**), indicating that zone refining is unlikely to significantly contribute to the gypsum composition, which in turn suggests limited precipitation-dissolution cycling. This is also in agreement with optical and electron microscopy, which does not show dissolution surfaces, but rather continuous growth of gypsum laths with idiomorphic growth surfaces preserved within individual gypsum crystals. There is, therefore, no evidence for gypsum dissolution, which is surprising given the abundance of rain and the resulting effect of dilution on the saturation state of the seepage fluids, and the gypsum dissolution rates determined by Zaier et al. (2020). This strongly suggests that dissolution is hindered. Still, even if pre-existing gypsum does not dissolve, no gypsum will precipitate when the fluids are undersaturated, and the gypsum record will therefore reflect only part of the year. The continuous growth model applied to the transect to obtain absolute ages can therefore only be interpreted up to a yearly resolution.

Equilibrium partition coefficients depend on physical conditions (e.g., P and T) and the major element compositions of the mineral and fluid (see van Hinsberg et al., 2010a and references therein). Under disequilibrium conditions, element partitioning will moreover depend on kinetic factors, including growth rate. There is no evidence to assume that seepage outflow temperatures changed significantly, with 1993–1996

temperatures reported by Delmelle and Bernard (2000) the same as our 1999 and 2007–2009 measurements. The major element composition of gypsum does not change along the transect, and the noble-gas corrected ^{210}Pb ages suggest a steady growth rate throughout. Measured variability in major element composition of the fluid results from variable dilution with only minor variability superimposed on top of this. Given that gypsum only precipitates once evaporation concentrates the fluid to gypsum saturation, variable dilution is likely inherently cancelled out. In conclusion, constant D-values can be assumed, and, hence, a constant and predictable incorporation of the fluid compositional fingerprint by gypsum. Together with the apparent lack of reworking, this makes gypsum a reliable archive of the seepage water composition.

Gypsum Transect Time Period

The oldest growth zone for the gypsum transect formed in 1919 ± 12 years as estimated from the 2 mm/yr growth rate determined from the noble gas corrected ^{210}Pb age model. This age is similar to the maximum age determined from visit reports and photographs from the 1920s, and would suggest the sampled section represents the full history of the plateau. It is unclear what changed in the 1920s to lead to formation of the plateau. Gypsum precipitates have been reported from the lake and Banyu Pait river valley as early as 1789 (Oudgast, 1820), and are mentioned by Stöhr in 1858 (Stohr, 1862), but the plateau appears to be more recent. Construction of a dam in the 1920s involved significant movement of material in the uppermost section of the Banyu Pait valley, just below the dam, and it is conceivable that this changed the seepage patterns. Whereas seepage was reported just below the dam for the earliest dam iterations leading to undercutting (see Hengeveld, 1920), this appears not to have been the case for later dams, where seepage moved further downstream.

Compositional History

The fluid compositional record can be reconstructed from approximately 1920–2008 by combining the element partition coefficients with the gypsum transect analyses. This record reflects two fluid sources as identified from the parallel trends in noble gas corrected ^{210}Pb (Figure 7). Moreover, absolute concentrations in the fluid will have varied with the degree of evaporative concentration of the fluid, or their dilution by ground and rainwater. The latter effect can be removed by dividing by a conservative element, and Sr has been chosen here for this purpose. Comparing the Sr-normalized compositions for the intervals representing the two fluid sources as identified by ^{210}Pb shows that there is no statistically significant difference between these fluids at the 5% confidence level (Mann-Whitney test of equality of medians), indicating that the two fluid sources dominantly differed in their absolute concentrations and that this difference is removed by dividing by Sr. This allows for the Sr-divided transect data to be interpreted as a single record.

Figure 8 shows the timeseries for a range of elements next to photographs of the gypsum transect. The most prominent features are the higher values for most elements around 1950, 1997, 2003, and 2006. The excursion around 1997 is particularly pronounced, for example in Cu/Sr. The 1997 and 2003 excursions

are of similar magnitude in Rb and Mg, whereas the 1997 excursion is larger for Cu and the 2003 one for Sb and As. This suggests that different processes controlled these excursions. Not all elements show these excursions; Pb and the LREE do not and form a separate compositional group. The overall trend among the LREE and Pb is similar, although the trough in Pb/Sr around 2003 is not observed for the LREE. Sr-normalized LREE and Pb are, in general, higher where visible inclusion bands are present in the gypsum (e.g., in 1959, 1982, 1993, 2007; Figure 8), but this is not a perfect correlation (e.g., in 1940). The other elements do not show a correlation with inclusion bands for these inclusions-filtered gypsum analyses, but a correlation is present for the data derived from the full integration windows.

The gypsum-fluid partition coefficients can be used to determine the susceptibility of the elements to compositional overprinting by inclusions. Inclusions are predominantly variably-altered rock fragments, plant debris and minerals including syngenite, barite and (Na,K)-alum. Solid/fluid D-values for Kawah Ijen basalt, andesite, dacite, strongly altered dacite, and (Na,K)-alum are shown in Figure 4A, as well as D-values for Ba, Sr and Pb for barite (data for solid and fluid phases from van Hinsberg et al. (2010b); van Hinsberg et al. (2010c); van Hinsberg et al. (2017), no trace element data are available for syngenite or plant debris). Rock fragments in the gypsum are mostly variably altered dacite, with subordinate basalt and andesite. Analyses for elements that are incompatible in gypsum, and that have a high concentration in the inclusion phases (represented by a D-value significantly higher than the D-value of gypsum) are most susceptible to modification. These elements therefore need to be interpreted with caution, and include the alkalis, Mg, Mn, and Ba. The HREE are more susceptible than the LREE, and co-variation of Ba, Sr and Pb would be indicative of barite contamination. Overall, the LREE, Sr, Pb, Tl, Ni, Co, Cu, Zn, Cd, Sb, Th, and Mo are least susceptible to inclusions, and therefore provide the best record of the fluid compositions from which the gypsum grew. We will restrict our interpretation to these elements in the following.

Controls on Seepage Water Compositions

The seepage spring waters are predominantly derived from the crater lake as evidenced by their near-identical conservative element ratios (Palmer, 2009). However, Utami et al. (2019) show that the rapid variability observed in the gypsum record can only be explained if an additional source of fluid is present locally, because the long residence time of elements in this large volume of brine means that it takes considerable time for compositional disturbances to be visible in the overall lake water composition (cf. Rouwet and Tassi, 2011). Gas bubbling is observed in the lake just in front of the dam, and the conservative element ratios in the various seepage springs suggest a 5% contribution from a different source than the lake (Palmer, 2009). Local groundwater is unable to change elemental ratios as it is too dilute, which suggests that this contribution is derived from the magmatic-hydrothermal system.

Of the most robust elements, LREE, Sr, and Pb are predominantly present in the Kawah Ijen acidic fluids as a
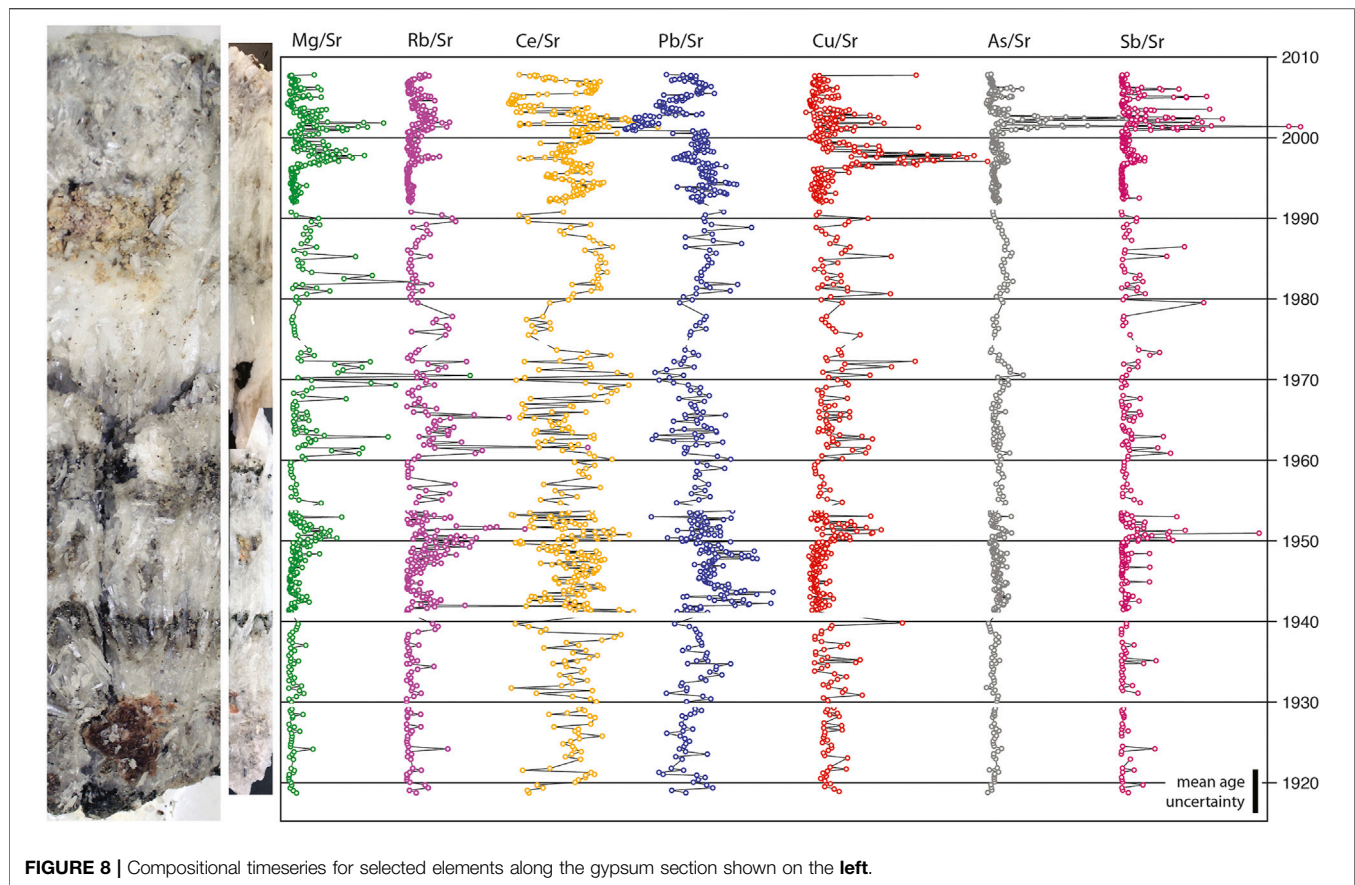
FIGURE 8 | Compositional timeseries for selected elements along the gypsum section shown on the **left**.

result of rock leaching, whereas Sb, Tl, and Cu are relatively enriched in its gaseous emissions (van Hinsberg et al., 2010b; van Hinsberg et al., 2017). Within the gaseous emissions themselves, Cu has been linked to destabilization of immiscible sulfide liquid in a deep-seated basaltic magma (together with Cd and Zn), whereas Sb and Tl, as well as, are associated with a shallower dacitic magma (Berlo et al., 2014). The behavior of Cu in the Kawah Ijen hydrothermal system is also affected by intermittent stability of a Cu-sulfide, as seen in monitoring of the Banyu Pait river water (Berlo et al., 2020). The behavior of the other (base) metals is not significantly impacted by this sulfide phase.

The gypsum timeseries shows covariation of the LREE and Pb, defining one compositional group, and covariation of Cu, Sb, Tl, As, Cd, and Zn in a second group (**Figure 8** and **Supplementary Figure S4**). This suggests a first-order signature in the timeseries that is related to rock-leaching and volcanic emissions, with little temporal overlap between these two processes. Within the metal group, Cu, Zn, and Cd show a more pronounced excursion in 1997 than in 2003, whereas Sb, Tl, and As show the reverse. This elemental grouping corresponds to that observed in melt inclusions and gas emissions by Berlo et al. (2014), which would indicate that the gypsum is recording varying contributions from the basaltic and dacitic magma bodies. It also matches the main difference in metal signature between modern and 1817 gypsum (Utami et al., 2019). Although the magnitude of Cu variation exceeds that of Zn and Cd, there is

strong co-variation among these elements, which suggests that intermittent Cu-sulfide stability does not contribute to the behavior of Cu at these uppermost seepage springs, possibly related to the absence of H_2S (see Berlo et al., 2014).

Utami et al. (2019) observed a similar grouping of the LREE + Pb, and the metals for their timeseries reconstructed from a Kawah Ijen gypsum stalactite. Separation within the metals is less clear in this timeseries. However, the foremost compositional signature in this stalactite is a bimodality in element variability, with low variance up to 1980, and high variance thereafter. Utami et al. (2019) interpreted this to represent an increase in particulates in the seepage fluids, and hence inclusions in the gypsum, as a result of the physical disturbances to the system as activity increased post-1980 (e.g., rock falls and lake sediment re-suspension). We do not observe the same bimodality in the plateau transect, although the most variability in composition is observed for the post-1990 period (**Figure 8**). This difference could reflect the different formation setting and conditions for the stalactites compared to the plateau. Whereas the plateau gypsum grows upward in pools, the stalactites form from water that flows over them and cools and evaporates as it does so.

Correlations With Volcanic Activity

Comprehensive monitoring of Kawah Ijen volcano has only commenced following unrest in 2010. The historical record of volcanic activity up to this point is incomplete and varies
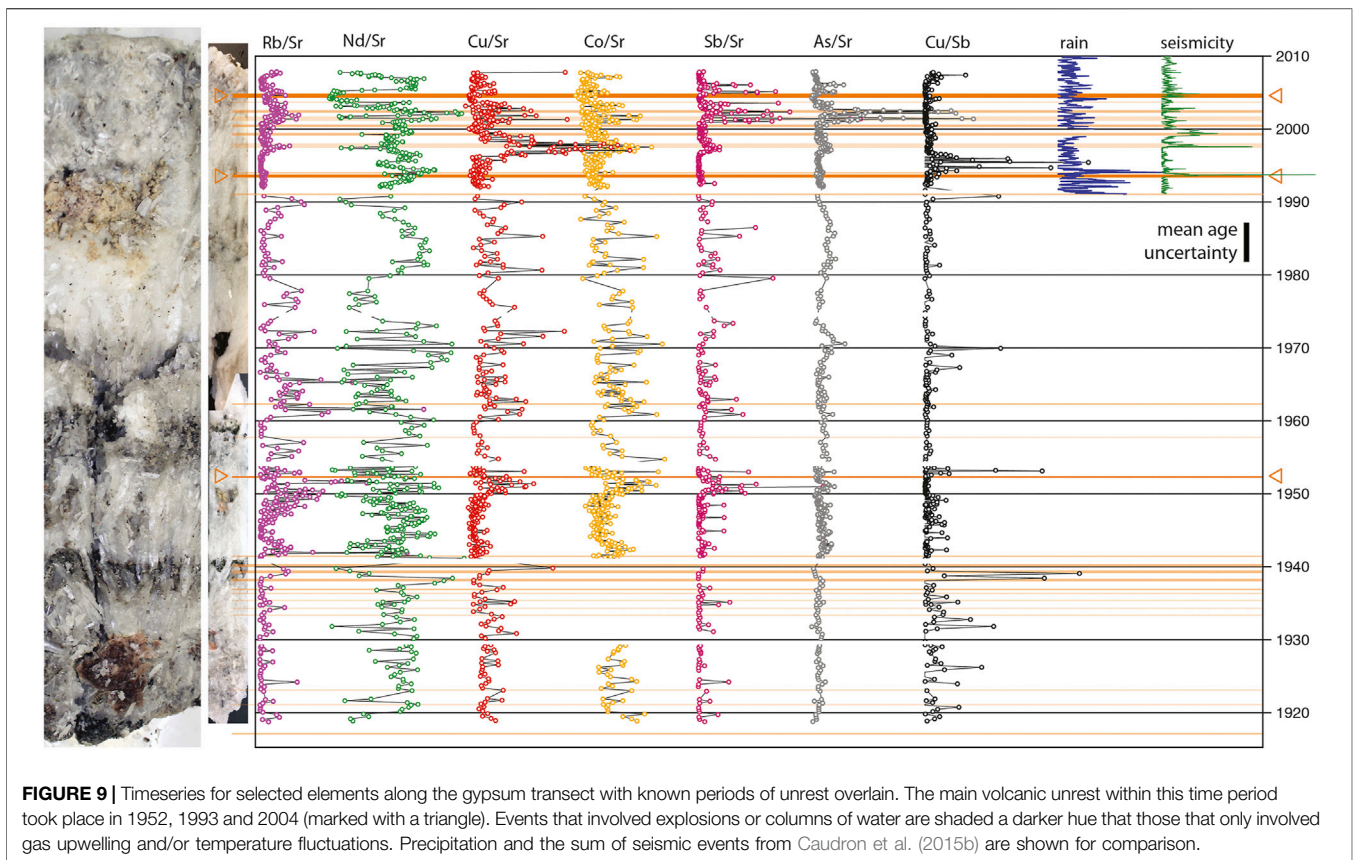
TABLE 5 | Summary of volcanic unrest reported for Kawah Ijen volcano, dominated by phreatic explosions and gas upwelling.

Year	Month	Main observations	Spilling	Event severity
1917	Feb-Mar	Temperature fluctuations; water thrown over dam	yes	medium
1921	Feb	Gas upwelling + "boiling"; Temperature rise	yes	low
1923	Mar	Temperature rise	?	low
1933	Apr	Temperature rise; gas upwelling	?	low
1934		Gas upwelling; Temperature rise	yes	low
1935		Temperature rise	?	low
1936	May	Temperature rise, gas upwelling	?	low
1936	Nov	Gas upwelling; Water fountains; Lake level fluctuations	?	medium
1938	Jan–Mar	Lake level fluctuations, Gas upwellingg, Temperature rise, Lake color white	?	medium
1939	Feb–Apr	Temperature rise; gas upwelling	?	low
1939	Apr	Temperature rise; gas upwelling	yes	low
1940	Feb-Mar	Temperature rise; gas upwelling	?	low
1941	Apr	Temperature rise; gas upwelling	yes	low
1952	Apr	Explosion and a 1 km tall plume	?	high
1957	Aug	Temperature rise; gas upwelling	?	low
1962	Apr	Gas slug explosions; Gas upwelling	?	medium
Lack of reports for the 1970s and 1980s				
1991	Mar-Apr	Gas explosions	no	medium
1993	Jul–Nov	Gas explosions and plume to 500 m	no	high
1994	Feb	Gas explosion	no	medium
1997	Jun-Dec	Seismicity	no	low
1999	Apr–Jun	Seismicity; Gas explosions	no	medium
2000	Jun–Sep	Plume to 25 m	no	medium
2001	Feb–Sep	Seismicity	no	low
2002	May–Aug	Seismicity; Small plumes	no	medium
2003	Oct	Seismicity	no	low
2004	May–Dec	Seismicity; Gas upwelling	no	high
Lull in activity from 2004 to 2010				
2011–2012		Seismicity, Temperature fluctuations, Gas upwelling	no	high

In a number of cases, the activity accompanied lowering of the lake level during intentional dam spilling, and was likely triggered by this. A spilling trigger was no longer present in the 1990s and 2000s because the water level was below that of the dam and no spilling took place. The assigned severity of unrest is relative, and no major events took place within the time period covered by the gypsum transect. Data from Caudron et al. (2015b) and references therein. Activity records for Kawah Ijen are incomplete and reporting strongly varies in detail.

significantly in the level of detail of reporting (Caudron et al., 2015b). This complicates developing an accurate record of volcanic activity at Kawah Ijen, and hinders comparing reported activity and establishing the significance of events. Small phreatic events appear to take place every year, and are reported as early as the 1900s (Kemmerling, 1921). They may result from lake overturn following development of stratification during the rainy season (Caudron et al., 2017). These smaller events include steam explosions, bubbling, rapid temperature and lake level variations and small phreatic plumes (see the overview in Caudron et al. (2015b). In part, lowering of the lake level during dam spilling periods triggered these events. Tourism and sulfur mining in the crater ensure that these events are witnessed at present, but given that these events are generally restricted to the lake and crater, could have easily gone unreported in the past. Overall, the most significant events since the start of the 20th century appear to have been phreatic unrest in 1952 in which a plume rose to 1 km height, phreatic steam explosions and a 500 m plume in 1993, unrest in 2004 with gas upwelling and increased seismicity and the seismicity crisis of 2011–2012 (**Table 5**, Caudron et al., 2015b). No reports are available for the 1970s and 1980s and this time period is therefore commonly regarded as a period of relative quiescence, but it is unclear to what extent this rather owes to a lack of available reports. The Ijen volcano observer, who has worked at the Ijen observatory since the 1980s regards the unrest of 1993 and 2004 as the most significant (Caudron et al., 2015b).

Figure 9 shows the episodes of volcanic unrest overlain on the compositional transect. The period of unrest in the late 1930s appears to correlate with a layer of debris in the gypsum, and this is also the case for the 1952 activity and that in the 2000s when some leeway in positioning is taken into account owing to the uncertainty in the absolute age assignment. The debris horizons around 1970 and 1985 do not correspond to known activity. The debris consists of variably altered rock fragments and organic material and is the same as material that is locally present on the slopes of the Banyu Pait valley. We therefore interpret it to represent local mobilization of material that is deposited onto the gypsum plateau. Volcanic activity resulted in material transfer over the dam in the past, although there is no mention of this after 1917. More likely, correlations with unrest result from rock falls and slides that accompanied the volcanic seismicity. Major rainstorms could have achieved the same, which can explain the presence of debris horizons where no activity was recorded. Indeed, it is known that severe rainstorms are common, and if anything, it is surprising that there are not more such horizons. The present-day plateau surface is mostly free of rock-fragments (**Figures 2**, **3**), despite the presence of loose material right next to the gypsum (e.g., **Figure 2C**). Perhaps, rainstorms, and dam spilling flush the plateau clean of debris, and it is only when rapid growth consolidates this debris that it is preserved. This could be verified in a visit during the rainy season. Such a visit would also be highly desirably to understand the apparent lack of gypsum

FIGURE 9 | Timeseries for selected elements along the gypsum transect with known periods of unrest overlain. The main volcanic unrest within this time period took place in 1952, 1993 and 2004 (marked with a triangle). Events that involved explosions or columns of water are shaded a darker hue that those that only involved gas upwelling and/or temperature fluctuations. Precipitation and the sum of seismic events from Caudron et al. (2015b) are shown for comparison.

dissolution during times of rain-diluted undersaturation of the seepage fluids.

Comparing the activity record to the timeseries for the elements that are least susceptible to overprinting shows correlations between the records (**Figure 9**). The large 1952 event corresponds to a peak in Sr-normalized Cu, Co, Sb, and As, and these same elements are high for the activity in the 1990s and 2000s. However, the large 1993 event does not appear to be present in the record and the largest excursion in Cu matches with what is only regarded as a minor event. This mismatch could be the result of the uncertainty in the absolute age assignment, and the 1993 event matches the Cu excursion within age uncertainty.

To determine whether there is a statistically significant signature of volcanic activity in the gypsum record, we conducted a PLS-DA analysis on the timeseries. Given the uncertainty in the absolute ages, the timeseries was smoothed with a 5-years moving average and each period of volcanic activity compared at intervals of 5 years (e.g. 1945 ± 2.5 years as a quiet period and 1950 ± 2.5 years as a period of unrest). The period from 1970 to 1980 was not included as it is unclear if no activity took place, or it was not reported. The PLS-DA analysis indicates that periods of activity can be separated from those of quiescence, with the LREE and then Zn the most important variables in this separation. The LREE are lower for periods of activity, whereas Zn is higher (**Figure 10**). Only one time period is assigned wrongly, 1960. We classified this as a period of activity given the gas slug explosions reported for April 1962, but the PLS-DA groups it with the quiescent time periods. Given that the smoothing and binning

removes most of the detail in the timeseries, this is a surprisingly clear result, and a strong indicator that active periods do have a distinct compositional signature that is recorded, and identifiable in the gypsum. When the resulting model is applied to the 1970s and 1980s, unrest is strongly predicted for the 1975 bin (the assignment has a score of 1.9 ± 1.1 with the cutoff between unrest and quiescence at 0). This suggests that there may have been an episode of unreported unrest in this time period.

A record of seismicity, lake temperature and precipitation is available from 1991 onward (Caudron et al., 2015b). To compare this dataset to the timeseries, we converted both to common time interval using linear interpolation, and the timeseries data were smoothed with a 5-years moving average window to account for the uncertainty in the absolute ages. No statistically significant correlations were found, and a visible inspection of the data confirms this (**Figure 9**). Rather than a lack of correlation, this may result from the uncertainty in the absolute age assignment.

Gypsum as a Recorder of Volcanic Activity at Kawah Ijen

The plateau gypsum timeseries provides a high-resolution record of volcanic activity at Kawah Ijen volcano. The element grouping observed corresponds to known element behavior at Kawah Ijen, and links to both rock leaching and volcanic contributions (*cf.* Berlo et al., 2014; Delmelle and Bernard, 1994; Takano et al., 2004; van Hinsberg et al., 2010b; van Hinsberg et al., 2017). Episodes of activity

FIGURE 10 | Boxplots showing a characteristic and statistically significant (at $\alpha = 5\%$) difference in Nd/Sr and Zn/Sr between active and quiet periods. The data were smoothed and binned in 5-years intervals to account for the uncertainty in absolute age assignment.
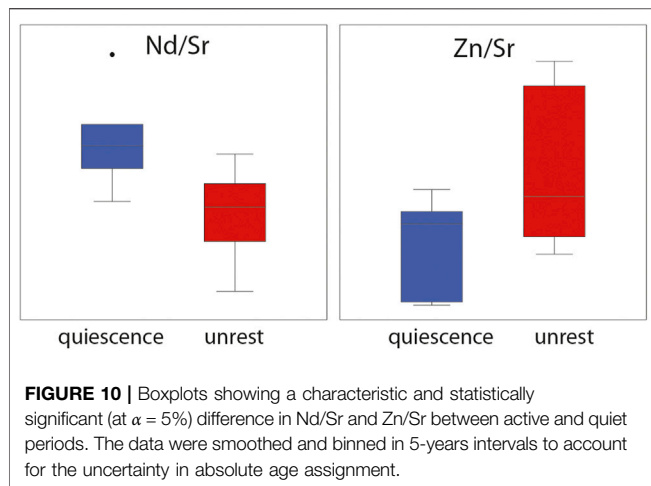
display a higher metal content in the gypsum, and, therefore, a higher content in the seepage waters (assuming constant partition coefficients). This metal enrichment is either dominated by Cu, Zn, and Cd, or by Sb, As, and Tl, suggesting two sources, whose contribution varies among events. The Cu, Zn, and Cd suite of elements has previously been linked to the deep-seated mafic magma at Kawah Ijen, whereas Sb, As, and Tl are characteristic of a shallower dacitic magma (Berlo et al., 2014). We therefore tentatively assign the Sb-As-Tl characterized events to the shallow magmatic-hydrothermal system, whereas Cu-Zn-Cd excursions would indicate involvement of a deeper source. Unfortunately, the uncertainty in absolute age assignment does not permit determining whether the larger events have a distinct signature, and a stronger contribution from either source. However, Utami et al. (2019) show that gypsum from the 1817 phreato-magmatic eruption of Kawah Ijen has a metal signature that fits the Cu-Zn-Cd suite, and for this eruption, involvement of the deeper reservoir is therefore likely. The cause for the strong negative correlation between activity and the LREE is unclear at present. The LREE derive predominantly from rock leaching, and Utami et al. (2019) show a positive correlation between activity and rock derived material, linked to increased rock falls and re-suspension of lake sediments as a result of physical disturbances of the system (i.e., seismicity). Takano et al. (2004) similarly suggest a positive correlation between REE contents and activity. Partition coefficients are particularly high for the LREE between gypsum and fluid. Possibly, the decrease in LREE content results from faster gypsum growth or higher water temperatures, both of which would lower partition coefficients.

CONCLUSION

- Gypsum provides a record of Kawah Ijen volcanic effluent from 1919 to 2008.
- Gypsum-fluid element partitioning indicates that the LREE, Sr, Pb, Ni, Co, Cu, Sb, Mo, and Th are least susceptible to overprinting by mineral and rock fragment inclusions, and are therefore the most robust indicators of changes in seepage fluid composition.

- Compositional variability correlates with known elemental sources and can be grouped in three elemental sets: LREE + Sr + Pb which represents a rock-leaching signature; Cu, Zn, Cd which suggests a source linked to deep-seated immiscible sulfide destabilization; and Sb, Tl, and As which point to a contribution from shallow evolved rocks.
- A distinct signature of volcanic unrest can be recognized in the gypsum composition, allowing for episodes of unrest and quiescence to be identified.
- Unambiguous linking of the compositional timeseries with existing records of volcanic unrest and seismicity are unfortunately hindered by uncertainty in the absolute age assignment, and a higher resolution age model is desired.
- Growth zoned gypsum is a reliable and robust recorder of fluid composition, and has the potential to provide a high-resolution record of volcanic activity. The Kawah Ijen compositional variability that it records also informs what elements are best suited to monitoring efforts.
- Gypsum is a common precipitate phase from volcanic brines (e.g., Poás volcano—Rodriguez and van Bergen 2017; Copahue Volcano—RodriguezVarekamp et al., 2016; Popocatépetl—Armienta et al., 2000; and Mount Ruapehu—Kilgour et al., 2010), and thus holds great promise as an archive of past volcanic activity where compositional preservation can be shown.

DATA AVAILABILITY STATEMENT

The original contributions presented in the study are included in the article/**Supplementary Material**, further inquiries can be directed to the corresponding author.

AUTHOR CONTRIBUTIONS

FUNDING

ACKNOWLEDGMENTS

SUPPLEMENTARY MATERIAL

The Supplementary Material for this article can be found online at: https://www.frontiersin.org/articles/10.3389/feart.2021.764087/full#supplementary-material

REFERENCES

Armienta, M. A., De la Cruz-Reyna, S., Macı́as, J. L., and Macias, J. (2000). Chemical characteristics of the crater lakes of Popocatetetl, El Chichon, and Nevado de Toluca volcanoes, Mexico. *J. Volcanology Geothermal Res.* 97, 105–125. doi:10.1016/s0377-0273(99)00157-2

Berlo, K., and Turner, S. (2010). 210Pb-226Ra Disequilibria in Volcanic Rocks. *Earth Planet. Sci. Lett.* 296, 155–164. doi:10.1016/j.epsl.2010.05.023

Berlo, K., van Hinsberg, V. J., Vigouroux, N., Gagnon, J. E., and Williams-Jones, A. E. (2014). Sulfide Breakdown Controls Metal Signature in Volcanic Gas at Kawah Ijen Volcano, Indonesia. *Chem. Geology.* 371, 115–127. doi:10.1016/j.chemgeo.2014.02.009

Berlo, K., van Hinsberg, V., SuparjanPurwanto, B. H., Purwanto, B. H., and Gunawan, H. (2020). Using the Composition of Fluid Seepage from the Magmatic-Hydrothermal System of Kawah Ijen Volcano, Indonesia, as a Monitoring Tool. *J. Volcanology Geothermal Res.* 399, 106899. doi:10.1016/j.jvolgeores.2020.106899

Bernatowicz, T. J., Podosek, F. A., Honda, M., and Kramer, F. E. (1984). The Atmospheric Inventory of Xenon and noble Gases in Shales: The Plastic Bag experiment. *J. Geophys. Res.* 89, 4597–4611. doi:10.1029/jb089ib06p04597

Blundy, J., and Wood, B. (2003). Partitioning of Trace Elements between Crystals and Melts. *Earth Planet. Sci. Lett.* 210, 383–397. doi:10.1016/s0012-821x(03)00129-8

Blundy, J., and Wood, B. (1994). Prediction of crystal-melt Partition Coefficients from Elastic Moduli. *Nature* 372, 452–454. doi:10.1038/372452a0

Bosch, C. J. (1858). Uitbarstingen der vulkanen Idjin en Raun (Banjoewangi). *Tijdschr. Ind. Taal-, Land- en Volkenkunde VII*, 265–286.

Brady, J. B., and Cherniak, D. J. (2010). 20. Diffusion in Minerals: An Overview of Published Experimental Diffusion Data. *Rev. Mineral. Geochem.* 72, 899–920. doi:10.1515/9781501508394-021

Capezzuoli, E., Gandin, A., and Pedley, M. (2014). Decoding Tufa and Travertine (Fresh Water Carbonates) in the Sedimentary Record: The State of the Art. *Sedimentology* 61, 1–21. doi:10.1111/sed.12075

Caudron, C., Campion, R., Rouwet, D., Lecocq, T., Capaccioni, B., Syahbana, D., et al. (2017). Stratification at the Earth's Largest Hyperacidic lake and its Consequences. *Earth Planet. Sci. Lett.* 459, 28–35. doi:10.1016/j.epsl.2016.11.002

Caudron, C., Lecocq, T., Syahbana, D. K., McCausland, W., Watlet, A., Camelbeeck, T., et al. (2015a). Stress and Mass Changes at a "wet" Volcano: Example during the 2011-2012 Volcanic Unrest at Kawah Ijen Volcano (Indonesia). *J. Geophys. Res. Solid Earth* 120, 5117–5134. doi:10.1002/2014jb011590

Caudron, C., Syahbana, D. K., Lecocq, T., van Hinsberg, V., McCausland, W., Triantafyllou, A., et al. (2015b). Kawah Ijen Volcanic Activity: a Review. *Bull. Volcanol* 77, 16. doi:10.1007/s00445-014-0885-8

Cogliati, S., Sherlock, S., Halton, A., Reid, K., Rymer, H., and Kelley, S. (2021). Tracking the Behaviour of Persistently Degassing Volcanoes Using noble Gas Analysis of Pele's Hairs and Tears: A Case Study of the Masaya Volcano (Nicaragua). *J. Volcanology Geothermal Res.* 414, 107212. doi:10.1016/j.jvolgeores.2021.107212

de la Tour, L. (1805). Notice sur un lac d'acide sulfurique qui se trouve au fond d'un volcan du Mont-Idienne, situe dans la province de Bagnia-Vangni, côte de l'ile de Java. *Ann. Mus. Hist. Nat.* 18, 425–446.

Delmelle, P., and Bernard, A. (2000). Downstream Composition Changes of Acidic Volcanic Waters Discharged into the Banyupahit Stream, Ijen Caldera, Indonesia. *J. Volcanology Geothermal Res.* 97, 55–75. doi:10.1016/s0377-0273(99)00159-6

Delmelle, P., and Bernard, A. (1994). Geochemistry, Mineralogy, and Chemical Modeling of the Acid Crater lake of Kawah Ijen Volcano, Indonesia. *Geochimica et Cosmochimica Acta* 58, 2445–2460. doi:10.1016/0016-7037(94)90023-x

Fairmaid, A. M., Kendrick, M. A., Phillips, D., and Fu, B. (2011). The Origin and Evolution of Mineralizing Fluids in a Sediment-Hosted Orogenic-Gold Deposit, Ballarat East, Southeastern Australia. *Econ. Geology.* 106, 653–666. doi:10.2113/econgeo.106.4.653

Fanale, F. P., and Cannon, W. A. (1971). Physical Adsorption of Rare Gas on Terrigenous Sediments. *Earth Planet. Sci. Lett.* 11, 362–368. doi:10.1016/0012-821x(71)90195-6

Gázquez, F., Bauska, T. K., Comas-Bru, L., Ghaleb, B., Calaforra, J.-M., and Hodell, D. A. (2020). The Potential of gypsum Speleothems for Paleoclimatology: Application to the Iberian Roman Humid Period. *Sci. Rep.* 10, 14705. doi:10.1038/s41598-020-71679-3

Giammanco, S., Sims, K. W. W., and Neri, M. (2007). Measurements of Rn-220 and Rn-222 and CO_2 Emissions in Soil and Fumarole Gases on Mt. Etna Volcano (Italy): Implications for Gas Transport and Shallow Ground Fracture. *Geochem. Geophys. Geosys* 8, Q10001. doi:10.1029/2007gc001644

Goede, A., and Vogel, J. C. (1991). Trace Element Variations and Dating of a Late Pleistocene Tasmanian Speleothem. *Palaeogeogr. Palaeoclimatol. Palaeoecol.* 88, 121–131. doi:10.1016/0031-0182(91)90018-m

Gunawan, H., Caudron, C., Pallister, J., Primulyana, S., Christenson, B., McCausland, W., et al. (2016). New Insights into Kawah Ijen's Volcanic System from the Wet Volcano Workshop experiment. *Geol. Soc. Lond. Sp Pub* 437, 1–22. doi:10.1144/sp437.7

Handley, H. K., Macpherson, C. G., Davidson, J. P., Berlo, K., and Lowry, D. (2007). Constraining Fluid and Sediment Contributions to Subduction-Related Magmatism in Indonesia: Ijen Volcanic Complex. *J. Petrol.* 48, 1155–1183. doi:10.1093/petrology/egm013

Hengeveld, G. J. N. (1920). De mogelijkheid en de plaats van den bouw van een nieuwe sluis bij het kratermeer Kawah Idjen. *Geologische onderzoekingen ten behoeve van 's lands waterstaat-, gewestelijke- en gemeentewerken in Nederlandsch Indie* 93–118.

Inguaggiato, C., Pappaterra, S., Peiffer, L., Apollaro, C., Brusca, L., De Rosa, R., et al. (2020). Mobility of REE from a Hyperacid Brine to Secondary Minerals Precipitated in a Volcanic Hydrothermal System: Kawah Ijen Crater lake (Java, Indonesia). *Sci. Total Environ.* 740, 140133. doi:10.1016/j.scitotenv.2020.140133

Jochum, K. P., Nohl, U., Herwig, K., Lammel, E., Stoll, B., and Hofmann, A. W. (2005). GeoReM: A New Geochemical Database for Reference Materials and Isotopic Standards. *Geostand Geoanalyt Res.* 29, 333–338. doi:10.1111/j.1751-908x.2005.tb00904.x

Kaneoka, I. (1994). "The Effect of Water on noble Gas Signatures of Volcanic Materials," in *Noble Gas Geochemistry*. Editor J. Matsuda (Tokyo: TERRAPUB), 205–215.

Kemmerling, G. L. L. (1921). *Het Idjen Hoogland. De geologie en geomorphologie van den Idjen. Koninklijke Natuurkundige Vereeniging Monografie II, Weltevreden-Batavia.* Batavia - Weltevreden: G. Kolff & Co, 134.

Kilgour, G., V. Manville, V., Pasqua, F. D., A. Graettinger, A., Hodgson, K. A., and Jolly, G. E. (2010). The 25 September 2007 Eruption of Mount Ruapehu, New Zealand: Directed Ballistics, Surtseyan Jets, and Ice-Slurry Lahars. *J. Volcanology Geothermal Res.* 191, 1–14. doi:10.1016/j.jvolgeores.2009.10.015

Lowenstern, J. B., van Hinsberg, V., Berlo, K., Liesegang, M., Iacovino, K., Bindeman, I. N., et al. (2018). Opal-a in Glassy Pumice, Acid Alteration,

and the 1817 Phreatomagmatic Eruption at Kawah Ijen (Java), Indonesia. *Front. Earth Sci.* 6, 475. doi:10.3389/feart.2018.00011

Matsubara, K., Matsuda, J.-i., Nagao, K., Kita, I., and Taguchi, S. (1988). Xe in Amorphous Silica: a New Thermometer in Geothermal Systems. *Geophys. Res. Lett.* 15, 657–660. doi:10.1029/gl015i007p00657

Matsuda, J.-i., and Nagao, K. (1986). Noble Gas Abundances in a Deep-Sea Sediment Core from Eastern Equatorial Pacific. *Geochem. J.* 20, 71–80. doi:10.2343/geochemj.20.71

Onuma, N., Higuchi, H., Wakita, H., and Nagasawa, H. (1968). Trace Element Partition between Two Pyroxenes and the Host Lava. *Earth Planet. Sci. Lett.* 5, 47–51. doi:10.1016/s0012-821x(68)80010-x

Oudgast (1820). *Mengelingen*, 7. Batavia: Bataviasche Courant.

Ozima, M., and Podosek, F. A. (1983). *Noble Gas Geochemistry*. Cambridge: Cambridge University Press, 367.

Palmer, S. (2009). *Hydrogeochemistry of the Upper Banyu Pahit River valley, Kawah Ijen Volcano, Indonesia*. Montreal, Canada: MSc thesis, McGill University, 114.

Paton, C., Hellstrom, J., Paul, B., Woodhead, J., and Hergt, J. (2011). Iolite: Freeware for the Visualisation and Processing of Mass Spectrometric Data. *J. Anal. Spectrom.* 26, 2508–2518. doi:10.1039/c1ja10172b

Pfann, W. G. (1962). Zone Melting. *Science* 135, 1101–1109. doi:10.1126/science.135.3509.1101

Pinti, D. L., Wada, N., and Matsuda, J.-i. (1999). Neon Excess in Pumice: Volcanological Implications. *J. Volcanology Geothermal Res.* 88, 279–289. doi:10.1016/s0377-0273(99)00006-2

Pitre, F., and Pinti, D. L. (2010). Noble Gas Enrichments in Porewater of Estuarine Sediments and Their Effect on the Estimation of Net Denitrification Rates. *Geochimica et Cosmochimica Acta* 74, 531–539. doi:10.1016/j.gca.2009.10.004

Rodríguez, A., and van Bergen, M. J. (2017). Superficial Alteration Mineralogy in Active Volcanic Systems: An Example of Poás Volcano, Costa Rica. *J. Volcanology Geothermal Res.* 346, 54–80. doi:10.1016/j.jvolgeores.2017.04.006

Rodríguez, A., Varekamp, J. C., van Bergen, M. J., Kading, T. J., Oonk, P., Gammons, C. H., et al. (2016). "Acid Rivers and Lakes at Caviahue-Copahue Volcano as Potential Terrestrial Analogues for Aqueous Paleo-Environments on Mars," in *Copahue Volcano. Active Volcanoes of the World*. Editors F. Tassi, O. Vaselli, and A. Caselli (Berlin, Heidelberg: Springer). doi:10.1007/978-3-662-48005-2_7

Rouwet, D., and Tassi, F. (2011). Geochemical Monitoring of Volcanic Lakes. A Generalized Box Model for Active Crater Lakes. *Ann. Geophys.* 54, 161–173. doi:10.4401/ag-5035

Shannon, R. D. (1976). Revised Effective Ionic Radii and Systematic Studies of Interatomic Distances in Halides and Chalcogenides. *Acta Cryst. Sect A.* 32, 751–767. doi:10.1107/s0567739476001551

Sitorus, K. (1990). *Volcanic Stratigraphy and Geochemistry of the Idjen Caldera Complex, Indonesia*. Wellington, New Zealand: MSc thesis, University of Wellington, 148.

Smith, S. P., and Kennedy, B. M. (1983). The Solubility of noble Gases in Water and in NaCl Brine. *Geochimica et Cosmochimica Acta* 47, 503–515. doi:10.1016/0016-7037(83)90273-9

Staudacher, T., and Allègre, C. J. (1982). Terrestrial Xenology. *Earth Planet. Sci. Lett.* 60, 389–406. doi:10.1016/0012-821x(82)90075-9

Stöhr, E. (1862). Der Vulkan Idjen in Ost-Java. *Verhandelingen van het Koninklijk Bataviaasch Genootschap der Kunsten en Wetenschappen* 7, 30–47.

Sumarti, S. (1998). *Volcanic Pollutants in Hyperacid River Water Discharged from Ijen Crater lake, East Java, Indonesia*. Utrecht, Netherlands: MSc thesis. Utrecht University.

Symonds, R. B., Gerlach, T. M., and Reed, M. H. (2001). Magmatic Gas Scrubbing: Implications for Volcano Monitoring. *J. Volcanology Geothermal Res.* 108, 303–341. doi:10.1016/s0377-0273(00)00292-4

Takano, B., Fazlullin, S. M., and Delmelle, P. (2000). Analytical Laboratory Comparison of Major and Minor Constituents in an Active Crater lake. *J. Volcanology Geothermal Res.* 97, 497–508. doi:10.1016/s0377-0273(99)00171-7

Takano, B., Suzuki, K., Sugimori, K., Ohba, T., Fazlullin, S. M., Bernard, A., et al. (2004). Bathymetric and Geochemical Investigation of Kawah Ijen Crater lake, East Java, Indonesia. *J. Volcanology Geothermal Res.* 135, 299–329. doi:10.1016/j.jvolgeores.2004.03.008

Torgersen, T., Kennedy, B. M., and van Soest, M. C. (2004). Diffusive Separation of noble Gases and noble Gas Abundance Patterns in Sedimentary Rocks. *Earth Planet. Sci. Lett.* 226, 477–489. doi:10.1016/j.epsl.2004.07.030

Utami, S. B., van Hinsberg, V. J., Ghaleb, B., and Pinti, D. L. (2019). Growth-zoned gypsum Stalactite from the Kawah Ijen Volcanic lake, Indonesia, Records a >40-year Record of Volcanic Activity. *Bull. Volcanol* 81, 52. doi:10.1007/s00445-019-1314-9

Utami, S. B., van Hinsberg, V. J., Ghaleb, B., and van Dijk, A. E. (2020). Oxygen Isotope Fractionation between gypsum and its Formation Waters: Implications for Past Chemistry of the Kawah Ijen Volcanic lake, Indonesia. *Am. Mineral.* 105, 756–763. doi:10.2138/am-2020-7298

van Hinsberg, V., Berlo, K., and Lowenstern, J. (2020). An Experimental Investigation of Interaction between Andesite and Hyperacidic Volcanic Lake Water. *Minerals* 10, 96. doi:10.3390/min10020096

van Hinsberg, V., Berlo, K., Sumarti, S., van Bergen, M., and Williams-Jones, A. (2010b). Extreme Alteration by Hyperacidic Brines at Kawah Ijen Volcano, East Java, Indonesia: II. *J. Volcanology Geothermal Res.* 196, 169–184. doi:10.1016/j.jvolgeores.2010.07.004

van Hinsberg, V., Berlo, K., van Bergen, M., and Williams-Jones, A. (2010c). Extreme Alteration by Hyperacidic Brines at Kawah Ijen Volcano, East Java, Indonesia: I. Textural and Mineralogical Imprint. *J. Volcanology Geothermal Res.* 198, 253–263. doi:10.1016/j.jvolgeores.2010.09.002

van Hinsberg, V. J., Migdisov, A. A., and Williams-Jones, A. E. (2010a). Reading the mineral Record of Fluid Composition from Element Partitioning. *Geol* 38, 847–850. doi:10.1130/g31112.1

van Hinsberg, V., Vigouroux, N., Palmer, S., Berlo, K., Mauri, G., Williams-Jones, A., et al. (2017). "Element Flux to the Environment of the Passively Degassing Crater lake-hosting Kawah Ijen Volcano, Indonesia, and Implications for Estimates of the Global Volcanic Flux," in *Geochemistry and Geophysics of Active Volcanic Lakes*. Editors T. Ohba, B. Capaccioni, and C. Capaccioni (London: Geological Society, Special Publications), 437, 9–34.

van Rotterdam-Los, A. M. D., Vriend, S. P., van Bergen, M. J., and van Gaans, P. F. M. (2008). The Effect of Naturally Acidified Irrigation Water on Agricultural Volcanic Soils. The Case of Asembagus, Java, Indonesia. *J. Geochemical Exploration* 96, 53–68. doi:10.1016/j.gexplo.2007.07.003

Vigouroux, N. (2011). *Tracking the Evolution of Magmatic Volatiles from the Mantle to the Atmosphere Using Integrative Geochemical and Geophysical Methods*. Vancouver, Canada: PhD thesis Simon Fraser University, 265.

Yudiantoro, D. F., Irawan, B. A., Haty, I. P., Sayudi, D. S., Suproboriniaru, A., Sekarwati, B., et al. (2020). Geochemistry Acidic Water of Banyupait River Effect Seepage of Crater Water Ijen Volcano, Asembagus, Situbondo, East Java, Indonesia. *Preprints.* doi:10.20944/preprints202008.0344.v1

Zaier, I., Billiotte, J., Charmoille, A., and Laouafa, F. (2020). The Dissolution Kinetics of Natural gypsum: a Case Study of Eocene Facies in the north-eastern Suburbs of Paris. *Env Earth Sci.* 80, 1–16. doi:10.1007/s12665-020-09275-x

Zimmer, M., and Erzinger, J. (2003). Continuous H2O, CO2, 222Rn and Temperature Measurements on Merapi Volcano, Indonesia. *J. Volcanology Geothermal Res.* 125, 25–38. doi:10.1016/s0377-0273(03)00087-8